Spin amplification in realistic systems

Ivan Iakoupov,[1,2,*] Victor M. Bastidas,[2] Yuichiro Matsuzaki,[2,3] Shiro Saito,[2] and William J. Munro[1,2]

[1]*Quantum Engineering and Design Unit, Okinawa Institute of Science and Technology Graduate University, 1919-1 Tancha, Onna-son, Okinawa 904-0495, Japan*

[2]*Basic Research Laboratories, NTT, Inc., 3-1 Morinosato-Wakamiya, Atsugi, Kanagawa 243-0198, Japan*

[3]*Department of Electrical, Electronic, and Communication Engineering, Faculty of Science and Engineering, Chuo University, 1-13-27 Kasuga, Bunkyo-ku, Tokyo 112-8551, Japan*

(Received 18 September 2024; accepted 14 July 2026; published 26 August 2026)

Spin amplification is the process that ideally increases the number of excited spins when one of them is excited initially. We show that by applying optimal control techniques to design classical drive pulse shapes, spin amplification can be achieved in a previously unexplored fast regime, with amplification times comparable to the intrinsic interaction timescale. This is an order of magnitude faster than the previous protocols and makes spin amplification possible even with significant decoherence and inhomogeneity in the spin system. The initial spin excitation can be delocalized over the entire ensemble, which is a more typical situation when a photon is collectively absorbed by the spins. We focus on the superconducting persistent-current artificial atoms and the Rydberg atoms as spins.

DOI: 10.1103/4nqk-9t5s

I. INTRODUCTION

Control of ever larger quantum systems is essential for quantum simulation [1–4], quantum sensing [5–8], and error-corrected quantum computing [9–11]. Such quantum systems can be viewed as collections of spins encoded in real or artificial atoms. Instead of aiming to deliver a separate driving field for each spin, experimental complexity could be decreased by using a global drive for the entire spin ensemble [12–23]. Addressing the individual spins or spin groups can then be done by frequency or polarization selectivity and engineering of the spin-spin interactions.

One of the operations that is useful for quantum sensing is spin amplification [23–25], which can be implemented with a global drive [17–19]. The idealized version of this operation amplifies a single excited spin into many excited spins, while keeping the ensemble with zero excited spins unchanged [see Fig. 1(a)]. This can be realized using the transverse-field Ising model with nearest-neighbor interactions. A continuous-wave weak classical field is applied such that it is off resonant with the frequency of the spins. One excited spin shifts the frequency of the neighboring spins into resonance with the drive, making a domain wall propagate in such a way that the number of the excited spins is increased [17–19,23,26].

The transverse-field Ising model can be implemented on general-purpose quantum computers [4], but this requires individual drives for the spins. In contrast, ensembles of Rydberg atoms, for instance, implement this model while utilizing a global drive [2,3]. An implementation of the transverse-field Ising model can also be achieved by the ensembles of superconducting persistent-current artificial atoms [27,28]. Compared to other superconducting artificial atoms with much better coherence properties [29–32], the primary advantage of the persistent-current artificial atoms is the small size that permits fabrication of thousands of spins on a compact chip [33]. Their large anharmonicity makes it possible to treat them as two-level systems even with strong drives, although large anharmonicities could also be obtained with, for instance, fluxonium [31] at the cost of a larger footprint. Due to being related to the persistent-current artificial atom, fluxonium can also have native ZZ interactions [34]. This allows a fluxonium ensemble to be another possible implementation of the transverse-field Ising model.

Realistic spin systems have imperfections, such as long-range interactions, finite lifetimes, and inhomogeneous broadening [2,3,33,35]. The position of the initial single excitation can be delocalized over the entire ensemble due to spins collectively absorbing a photon [36,37]. Designing a protocol to amplify such delocalized states using imperfect spins is difficult to do manually. Therefore, we turn to optimal control [38] to replace the weak continuous-wave drive field with a time-dependent one that can be much stronger at its maximum.

The rest of the article is organized as follows. Our theoretical model and parameters are described in Sec. II with the results presented in Sec. III. The implications of the results are discussed in Sec. IV with a conclusion also provided.

II. SETUP

We focus on the two-dimensional (2D) layout of the spins (depicted schematically in Fig. 1) due to it being easily

*Contact author: ivan.iakoupov@oist.jp

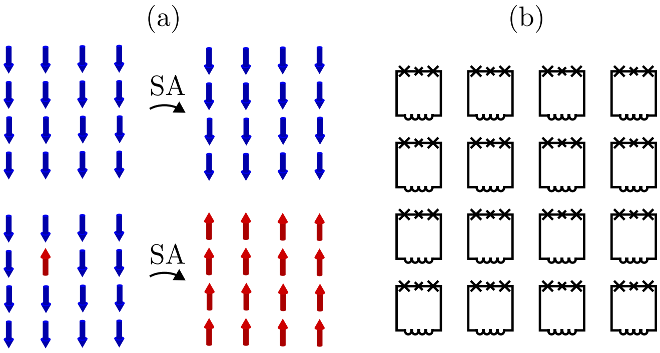

FIG. 1. (a) The idealized spin amplification (SA) operation. If all spins are in the ground state initially, there is no change (top). If one spin is excited initially, all spins become excited (bottom). We consider an equal superposition of all the single-excitation states instead of a particular excited spin position, as shown in the figure. (b) One of the considered experimental platforms: a 2D array of persistent-current artificial atoms [27] as the spin ensemble. The artificial atoms consist of superconducting loops interrupted by three Josephson junctions (crosses) where one of the junctions is smaller than the other two. The superconducting loops have linear inductance (inductors at the bottom of the loops), and the interactions between the spins are due to the mutual inductance between the loops. The interactions are all-to-all in nature.

transferable to the experiments [2,3,33]. The spins are encoded either in the Rydberg atoms or in the persistent-current artificial atoms. The Hamiltonians for both systems are in the interaction picture with respect to the carrier frequency of the drive ω_d and use the rotating-wave approximation.

The Hamiltonian for the ensemble of the Rydberg atoms is

$$H_\mathrm{Ryd} = \hbar \sum_j (-\Delta \hat{n}_j + \Omega \hat{\sigma}_{x,j}) + \hbar \sum_{\substack{j,k \\ j\neq k}} J_{z,jk} \hat{n}_j \hat{n}_k, \qquad (1)$$

where $\hat{n}_j = |1\rangle\langle 1|_j = (1+\hat{\sigma}_{z,j})/2$ is the projector onto the excited state of the spin j ($\hat{\sigma}_{z,j}$ is the Pauli-Z operator), $\Delta = \omega_\mathrm{d} - \omega_{01}$ is the detuning between the transition frequency ω_{01} and ω_d, and $J_{z,jk} \propto r_{jk}^{-6}$, with r_{jk} being the distance between the spins j and k. The choices for the absent factor of 2 in the Ω term and double counting of the $J_{z,jk}$ terms (by not restricting $j < k$ in the summation) are different from Refs. [2,3], so rescaling of the parameters is necessary. Defining $J_{z,\mathrm{nn}}$ to be $J_{z,jk}$, where j and k are nearest neighbors, we therefore set $J_{z,\mathrm{nn}}/(2\pi) = 1\,\mathrm{MHz}$, and maximum Rabi frequency $\Omega/(2\pi) = 3.5\,\mathrm{MHz}$ [3]. Both the detuning Δ and the Rabi frequency Ω can be time dependent to perform optimal control of the Rydberg atoms [39]. The atoms are assumed to be trapped in a square grid with the nearest neighbors 10 μm apart [3]. The errors in positions have two components: the static trap position offset with the standard deviation of 100 nm, and the position of the atom within the trap due to the finite temperature with standard deviations of 170 nm in the plane of the array and 1 μm out of the plane [3]. These errors translate into inhomogeneity of the couplings $J_{z,jk}$.

The Hamiltonian for the ensemble of persistent-current artificial atoms is

$$H_\mathrm{PCAA} = -\hbar \sum_j \left(\frac{\Delta_j}{2} \hat{\sigma}_{z,j} + f_j \Omega \hat{\sigma}_{+,j} + f_j \Omega^* \hat{\sigma}_{-,j} \right) + \hbar \sum_{\substack{j,k \\ j\neq k}} J_{z,jk} \hat{\sigma}_{z,j} \hat{\sigma}_{z,k} + \hbar \sum_{\substack{j,k \\ j\neq k}} J_{\pm,jk} \hat{\sigma}_{+,j} \hat{\sigma}_{-,k}, \qquad (2)$$

where $\hat{\sigma}_{\pm,j}$ is the raising/lowering operator. In contrast to the Rydberg atoms, the transition frequencies $\omega_{01,j}$ and hence the detunings Δ_j are different for the different spins. They can be written as $\Delta_j = \Delta_\mathrm{avg} + \omega_{01,\mathrm{avg}} - \omega_{01,j}$, where $\omega_{01,\mathrm{avg}}$ is the average frequency (with averaging both over the spins in the ensemble and inhomogeneity realizations of the ensemble) and $\Delta_\mathrm{avg} = \omega_\mathrm{d} - \omega_{01,\mathrm{avg}}$. The Rabi frequency Ω can be time dependent and complex, with the real and imaginary parts corresponding to the I and Q signals.

The distributions of the parameters in the above Hamiltonian were calculated using circuit quantization, as described in Appendix A. The input parameters to this calculation are written in the caption of Fig. 2 that also shows the distributions graphically. For the chosen bias flux Φ_ext, the detunings $\Delta_j/(2\pi)$ have a standard deviation of 1.5 GHz, and the average transition frequency is $\omega_{01,\mathrm{avg}}/(2\pi) = 8.0\,\mathrm{GHz}$. The average transition frequency $\omega_{12,\mathrm{avg}}/(2\pi) = 32.2\,\mathrm{GHz}$ between the first and second excited states is only calculated to show that the anharmonicity is so large that the artificial atoms can be treated as two-level systems and is not used in the Hamiltonian (2).

Only the nearest-neighbor couplings $J_{\pm,\mathrm{nn,avg}}$ and $J_{z,\mathrm{nn,avg}}$ are shown in Fig. 2, but all the coupling strengths $J_{\pm,jk}$ and $J_{z,jk}$ in the Hamiltonian (2) are calculated based on the mutual inductance between the superconducting loops and then used in the simulations. The distribution of $J_{z,\mathrm{nn}}/(2\pi)$ has average $J_{z,\mathrm{nn,avg}}/(2\pi) = 39.8\,\mathrm{MHz}$ and standard deviation 4.4 MHz. The distribution of $J_{\pm,\mathrm{nn}}/(2\pi)$ has average $J_{\pm,\mathrm{nn,avg}}/(2\pi) = 6.1\,\mathrm{MHz}$ and standard deviation 3.6 MHz. We account for the small variations in the Rabi frequency for the different spins due to the inhomogeneity in the loop area by multiplying the ideal Rabi frequency Ω with time-independent factors f_j, which are equal to the ratio of the actual area of the superconducting loop to the design value. They have the average value 1 and standard deviation 0.0014.

The idealized transverse-field Ising model of Refs. [17–19] is obtained when couplings in the Hamiltonian (2) are such that $J_{\pm,jk} = 0$, and only the nearest neighbor $J_{z,jk}$ are nonzero. Note that the scaling of the Δ_j and $J_{z,jk}$ terms in Hamiltonian (2) is different from Refs. [17–19], and the choice of the scaling is different among those references. We also have the double counting of the terms $J_{z,jk}\hat{\sigma}_{z,j}\hat{\sigma}_{z,k}$ in the Hamiltonian (2). This was chosen for consistency with the summation over the terms $J_{\pm,jk}\hat{\sigma}_{+,j}\hat{\sigma}_{-,k}$, where no double counting occurs, because the operators for j and k are different. Both summations arise from the summation over the off-diagonal elements of the inductance matrix that is symmetric. Nonzero $J_{\pm,\mathrm{nn,avg}}$ is always present in the persistent-current artificial atoms.

For the chosen parameters, the flux bias $\Phi_\mathrm{ext} = 0.5034 \times \Phi_0$, where Φ_0 is the magnetic flux quantum, minimizes

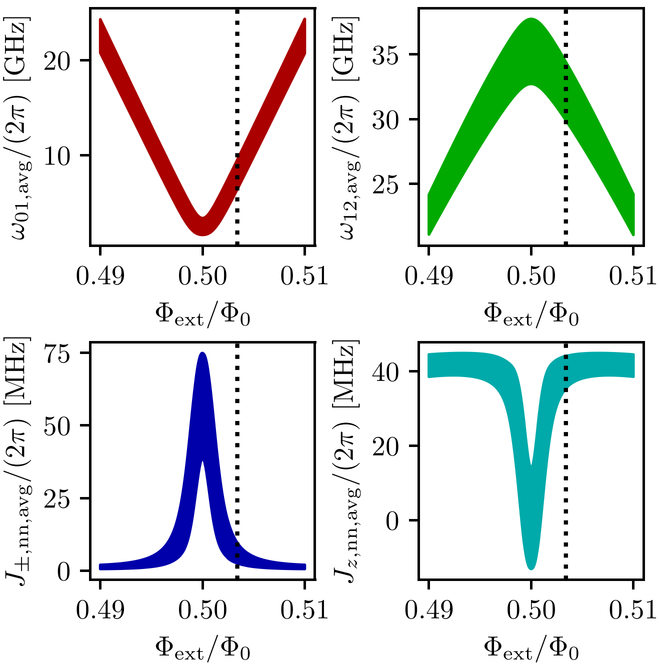

FIG. 2. The average parameters of the Hamiltonian (2) for the persistent-current artificial atoms [27] as spins: the transition frequencies between the ground and excited states $\omega_{01,\mathrm{avg}}$, the transition frequencies between the first and second excited states $\omega_{12,\mathrm{avg}}$, and the values of the nearest-neighbor couplings $J_{\pm,\mathrm{nn,avg}}$ and $J_{z,\mathrm{nn,avg}}$ ($J_{\pm,jk}$ and $J_{z,jk}$ with the maximal absolute values, respectively). Values for a range of bias fluxes $\Phi_{\mathrm{ext}}/\Phi_0$ are shown, where Φ_0 is the magnetic flux quantum. The curves are calculated by performing circuit quantization of the persistent-current artificial atoms with the Josephson-junction area error of 2% for 10^4 different realizations of a square 4×4 ensemble. The difference in the shown values between using 3×3 and 4×4 ensembles for averaging is small. The thickness of the curves shows the standard deviation of the parameters. The chosen $\Phi_{\mathrm{ext}}/\Phi_0 = 0.5034$ is shown by the black dotted vertical line. The parameters of the persistent-current artificial atoms are close to Ref. [40]: $E_J/h = 300$ GHz, $E_J/E_C = 75$, $\alpha = 0.7$ (relative area of the smaller junction). The model is extended to include the linear inductance, and the persistent-current artificial atoms are assumed to be square loops of size $3\,\mu\mathrm{m} \times 3\,\mu\mathrm{m}$ and use $0.2\,\mu\mathrm{m} \times 0.1\,\mu\mathrm{m}$ traces (width $\times$ height). The error in the side lengths of the loops is assumed to be 0.1%, and they are spaced $1\,\mu\mathrm{m}$ apart.

the inhomogeneous broadening due to the variations in the Josephson-junction area [40]. However, this is masked by the inhomogeneity due to variations in the loop area. While performing circuit quantization, small additional inhomogeneous broadening of Δ_j appears due to the long-range couplings, even in the absence of fabrication imperfections.

We consider two different initial states: the zero-excitation state

$$|\psi_0\rangle = \bigotimes_j |0_j\rangle \tag{3}$$

and the superposition of the single-excitation states

$$|\psi_1\rangle = \frac{1}{\sqrt{N}} \sum_j \hat{\sigma}_{+,j} |\psi_0\rangle, \tag{4}$$

which can be a result of N spins collectively absorbing a photon [36,37]. Unless noted otherwise, the results below focus on such a delocalized excitation, but we also briefly consider the localized initial state $|\psi_1\rangle = \hat{\sigma}_{+,j=1}|\psi_0\rangle$, with $j = 1$ being the corner spin [19]. The measurement operator for the population (total number) of the excited spins is $\hat{M} = \sum_j \hat{\sigma}_{+,j}\hat{\sigma}_{-,j}$. Writing the spin amplification operation as a superoperator $\mathcal{U}$, we thus maximize the expectation value

$$P_1 - P_0 = \mathrm{tr}[\hat{M}\mathcal{U}(|\psi_1\rangle\langle\psi_1|)] - \mathrm{tr}[\hat{M}\mathcal{U}(|\psi_0\rangle\langle\psi_0|)]. \tag{5}$$

This expectation value is the difference of excited-state populations and hence $-N \leqslant P_1 - P_0 \leqslant N$.

For the optimal control, the main parametrization of the Rabi frequency Ω in the Hamiltonians (1) and (2) that we use is based on the filtered piecewise-constant parametrization from Ref. [41]. Compared to the unfiltered piecewise-constant parametrization where penalty terms are added to make the pulses physically realizable, and the suitable constants multiplying the penalty terms are found by trial and error [42], embedding the constraints in the pulse parametrization itself [41] avoids the need for such tuning.

Gaussian filtering of the indicator functions

$$\mathbf{1}_{[a,b]}(t) = \begin{cases} 1, & \text{if } t \in [a, b], \\ 0, & \text{if } t \notin [a, b] \end{cases} \tag{6}$$

was experimentally verified to be a good model for the finite bandwidth of the arbitrary waveform generators [41]. Our only change of this parametrization is to use tanh function [which maps the real line onto the compact interval $(-1, 1)$] on every amplitude to additionally constrain the extremal values. This results in

$$\mathrm{Re}[\Omega](t) = \frac{\Omega_{\max}}{\sqrt{2\pi}\sigma} \int_{-\infty}^{\infty} \exp\left(-\frac{(t-t')^2}{2\sigma^2}\right) \times \sum_{p=1}^{N_c} \tanh(a_p) \mathbf{1}_{[(t_f/N_c)(p-1),(t_f/N_c)p]}(t')\mathrm{d}t', \tag{7a}$$

$$\mathrm{Im}[\Omega](t) = \frac{\Omega_{\max}}{\sqrt{2\pi}\sigma} \int_{-\infty}^{\infty} \exp\left(-\frac{(t-t')^2}{2\sigma^2}\right) \times \sum_{p=1}^{N_c} \tanh(b_p) \mathbf{1}_{[(t_f/N_c)(p-1),(t_f/N_c)p]}(t')\mathrm{d}t', \tag{7b}$$

where $\Omega_{\max}$ is the maximum absolute Rabi frequency. The integrals in Eq. (7) can be evaluated analytically in terms of the error functions [41]. The parametrization (7) is for the persistent-current artificial atoms, where the detunings are constant in time, and the I and Q parts of the microwave pulse are shaped. For the Rydberg atoms, Ω is real and positive, and Δ is changed in time [39]. To make Ω positive, we use the logistic function $\sigma(x) = 1/(1 + e^{-x})$ [which maps the real line onto the interval (0, 1)] instead of tanh in Eq. (7a) and take Eq. (7b) to mean the parametrization of $\Delta(t)$ instead of $\mathrm{Im}[\Omega](t)$ (replacing $\Omega_{\max}$ with $\Delta_{\max}$).

For the persistent-current artificial atoms, we assume the sampling rate of 10 GS/s [43] that determines N_c in Eq. (7) and the bandwidth $1/\sigma = 4$ GHz. In the case of the Rydberg atoms, the output of the arbitrary waveform generator is fed into an acousto-optic modulator [39], which determines the final bandwidth $1/\sigma$ of the pulses. We assume that $1/\sigma =$

25 MHz [44] in this case, and therefore the sampling rate is set to a lower value of 1 GS/s. To ensure that Ω is close to zero for $t = 0$ and $t = t_f$, we set a certain number of a_p and b_p to zero in the beginning and the end of the interval [41]. For this, we use a heuristic rule that a_p and b_p are set to zero for $p - 1$ below $4\sigma N_c/t_f + 1$ and above $N_c - 4\sigma N_c/t_f - 1$. For this, we use a heuristic rule that $a_p = 0$ and $b_p = 0$ with $p - 1$ below $4\sigma N_c/t_f + 1$ and above $N_c - 4\sigma N_c/t_f - 1$ are set to zero. This results in $|\Omega|/(2\pi), |\Delta|/(2\pi) < 0.5\,\mathrm{kHz}$ for $t = 0$ and $t = t_f$ in the pulse shapes for all the plots below.

We could not reach the theoretical bound $P_1 - P_0 = N$ with the parametrization (7), even when the other imperfections (finite coherence time, inhomogeneity) were removed from the model. Therefore, to check that this theoretical bound is indeed attainable, we also use the Fourier series parametrization [45]

$$\mathrm{Re}[\Omega_{\mathrm{Fourier}}](t) = \sqrt{\frac{2}{t_f}}\sum_{p=1}^{N_c} a_p \sin(\omega_p t), \tag{8a}$$

$$\mathrm{Im}[\Omega_{\mathrm{Fourier}}](t) = \sqrt{\frac{2}{t_f}}\sum_{p=1}^{N_c} b_p \sin(\omega_p t), \tag{8b}$$

where N_c is the number of the Fourier components and $\omega_p = p\pi/t_f$. The Rabi frequency is zero for the initial time $t = 0$ and the final time $t = t_f$. We set $N_c = 100$ so that it is large enough to parametrize pulses with bandwidth of several gigahertz for amplification times below 10 ns.

The initial states are propagated in time with either the Schrödinger or master equation using the fourth-order Runge-Kutta method. When evolving the master equation is too costly (many time steps or averaging over many inhomogeneity realizations), the ensembles with $N = 16$ spins are simulated using the quantum trajectory method [46]. In all cases, the full Hilbert space with the basis size 2^N is used, necessitating significant computational power already for modestly large ensembles.

The detuning Δ_{avg} from the average spin frequency is optimized together with the pulse shape parameters a_p and b_p. For the persistent-current artificial atoms, Δ_{avg} is one time-independent parameter, while for the Rydberg atoms, it is a time-dependent shape that is parametrized by the values b_p. Our optimal control approach is similar to Ref. [47], where the gradient of the final population difference (5) with respect to the pulse parameters is found using the reverse-mode automatic differentiation (cf. Appendix C) and then used in the Limited-memory Broyden-Fletcher-Goldfarb-Shanno (LBFGS) algorithm [48].

In contrast to the Gradient Ascent Pulse Engineering (GRAPE) method [49], where finding the exact gradient is computationally expensive and is often approximated for efficiency [41,50], the gradients of the Runge-Kutta methods can be calculated exactly with a small-constant overhead compared to the first-order (Euler method) approximation [47,51]. We use the fourth-order method similar to Ref. [47] instead of the second-order method of Ref. [51], because the higher order requires fewer time steps. In Appendix B, we detail an almost matrix-free operator approach that is more efficient than the sparse-matrix operators in Refs. [47,51] and can be used with any Runge-Kutta method. Matrix-free operators can also be used with the Krotov method [52], but its quasi-Newton extension (similar to Broyden-Fletcher-Goldfarb-Shanno (BFGS)) is not straightforward [53].

In our implementation, the total memory requirements for the optimal control are around 14.5 (18.5) times the size of the density matrix (state vector). The difference between the multiples for the density matrix and the state vector is that some auxiliary vectors have a fixed size equal to the state vector, and hence are negligible in size compared to the density matrix. Importantly, the memory requirements are independent of the number of the optimal control parameters and simulation time steps. The latter is achieved by propagating the final states backward in time during the gradient calculation [52,54]. This makes it possible to simulate and optimize the control pulse shapes for ensembles of up to $N = 16$ spins using the master equation.

The optimization method above is only guaranteed to converge to a local optimum, and we use the multistart approach to probabilistically explore more of the optimization landscape. For all the optimal control results, the pulse shapes are initialized randomly with each a_p and b_p sampled from the standard normal distribution (with mean 0 and standard deviation 1). Since different frequency scales are used for the two different kinds of spins that we consider, $\Delta_{\mathrm{avg}}/(2\pi \times 1\,\mathrm{MHz})$ is sampled from the standard normal distribution for the Rydberg atoms, and $\Delta_{\mathrm{avg}}/(2\pi \times 40\,\mathrm{MHz})$ is sampled for the persistent-current artificial atoms. We take ten such initial pulse realizations and pick the best optimized pulse shape as the result.

Rydberg atoms and persistent-current artificial atoms have significantly different couplings and coherence times. In both cases, the lifetime T_1 is relatively large, but the pure dephasing time T_ϕ is the limiting factor for the coherent operations. We set $T_1 = 175\,\mu\mathrm{s}$ and $T_\phi = 20\,\mu\mathrm{s}$ for the Rydberg atoms [3], and $T_1 = 1\,\mu\mathrm{s}$ and $T_\phi = 15$ ns for the persistent-current artificial atoms [35]. The persistent-current artificial atoms have a smaller coherence time, but they also have around 40 times larger interaction strengths and can be driven with stronger Rabi frequencies. This makes it possible to perform spin amplification much faster than with the Rydberg atoms.

In both cases, to perform the spin amplification approximately coherently, the amplification time t_f is chosen smaller than T_ϕ. We set $t_f = 1\,\mu\mathrm{s}$ for the Rydberg atoms and $t_f = 6.5$ ns for the persistent-current artificial atoms. For the latter, t_f is close to the timescale set by the nearest-neighbor interaction $1/|J_{z,\mathrm{nn}}| \approx 4$ ns. For the Rydberg atoms, t_f is limited by the maximal Rabi frequencies possible in the experimental setups, and hence does not approach $1/|J_{z,\mathrm{nn}}|$ as closely.

The previous spin amplification protocols [17–19,23] used a small-constant Rabi frequency $|\Omega| \ll |J_{z,\mathrm{nn}}|$ that resulted in amplification times much longer than $1/|J_{z,\mathrm{nn}}|$. This approach only works for long T_1 and T_ϕ. Finite T_ϕ makes the spin amplification slower [19] and also introduces erroneous excitations in the initial zero-excitation case as explained in Appendix D. Finite T_1 limits the total achievable excitation number in the single-excitation case. While choosing a larger $|\Omega|$ could partially compensate for this, this also increases the zero-excitation error due to the finite T_ϕ.

Since the largest contribution to the inhomogeneity in persistent-current artificial atoms stems from the geometric variations of the superconducting loops and hence is fixed after the fabrication, we optimize distinct pulse shapes for every inhomogeneity realization. In contrast, Rydberg atoms have a much smaller but dynamic inhomogeneity that stems from indeterminate positions of the atoms in the trap sites. Therefore, for the Rydberg atoms, the pulse shapes are optimized such that they work for any inhomogeneity realization with the average $P_1 - P_0$ being the target to optimize.

III. RESULTS

For a 2D homogeneous ensemble with the nearest-neighbor couplings, a two-frequency continuous-wave drive is sufficient [19]. Since the considered systems are inhomogeneous with long-range couplings, we follow the recommendation of Ref. [18] to increase the drive strengths, which may overcome frequency mismatch. This leads us to consider the baseline with the following time-dependent Rabi frequency:

$$\Omega(t) = \Omega_1 + \Omega_2 \exp(i(\Delta_{\text{avg},1} - \Delta_{\text{avg},2})t), \tag{9}$$

where the detuning $\Delta_{\text{avg},1} = \omega_{\text{d},1} - \omega_{01,\text{avg}}$ of the first frequency component is included in $\Delta_j = \Delta_{\text{avg},1} + \omega_{01,\text{avg}} - \omega_{01,j}$ in the Hamiltonian (2).

Optimizing over Ω_l and $\Delta_{\text{avg},l}$ for $l = 1, 2$ in Eq. (9) makes it a rudimentary form of optimal control. For every inhomogeneity realization of the persistent-current artificial atoms, we perform a global optimization with the algorithm DIRECT [55,56] inside the bounds $\Omega_l/(2\pi) \in [0.1, 2.4] \times 40\,\text{MHz}$, $\Delta_{\text{avg},l}/(2\pi) \in [-5, 5] \times 40\,\text{MHz}$, where 40 MHz is approximately equal to the nearest neighbor $|J_{z,jk}|/(2\pi)$ in Hamiltonian (2). The average values of the population differences $P_1 - P_0$ and error bars showing the standard deviations are shown as cyan squares in Fig. 3. The population differences $P_1 - P_0$ appear to reach a limit already for $N = 16$ with the value $P_1 - P_0 = 1.9 \pm 0.4$ (increasing less than 0.1 from $N = 9$). The optimal $\Omega/(2\pi) \approx |J_{z,\text{nn}}|/(2\pi) \approx 40\,\text{MHz}$ is outside of the parameter regime considered in Refs. [17–19].

Using optimal control with the parametrization (7) that has more frequency components and the gradient-based optimization improves the performance of spin amplification over the baseline above. More importantly, $P_1 - P_0$ increases with increasing N, even though the scaling is sublinear. The results are shown by blue circles in Fig. 3. The values for $N = 4$ and $N = 9$ were optimized using the master equation directly. For $N = 16$, a different approach was taken, and the value $P_1 - P_0 = 5.7 \pm 0.9$ is not fully optimized. The pulse shapes were found using the Schrödinger equation but with retained parameter inhomogeneity, which is the most important imperfection. These pulse shapes were then evaluated using the master equation to obtain the blue circle for $N = 16$ in Fig. 3. Optimizing all of the 100 inhomogeneity realizations with the master equation is too computationally expensive. On dual AMD Epyc 9554 CPUs (128 cores in total), one iteration takes around 90 h with 817 simulation time steps. The number of time steps is double that of the homogeneous-ensemble results below to prevent numerical instability caused by the large inhomogeneity in the parameters. We have chosen 3 realizations that were optimized for 19 iterations each. This has improved $P_1 - P_0$ for this subset of realizations from 5.9 ± 0.7 to 6.1 ± 0.7.

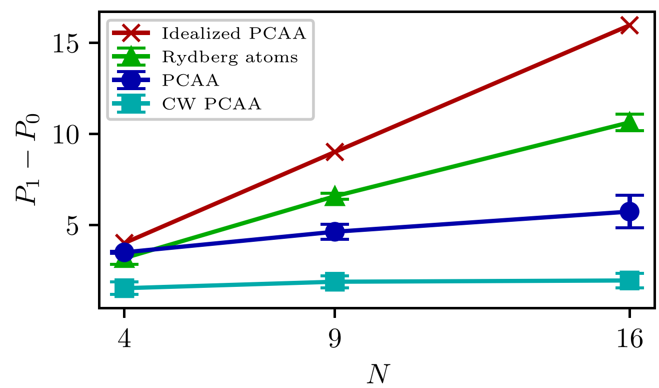

FIG. 3. Difference of the final populations $P_1 - P_0$ for the spin amplification as a function of the number of spins N. The results are for two types of spins: Rydberg atoms and persistent-current artificial atoms (PCAA). For the continuous-wave (CW) PCAA results (cyan squares), the two-frequency parametrization (9) is used for the Rabi frequency with optimized [55,56] Ω_1, Ω_2, $\Delta_{\text{avg},1}$, and $\Delta_{\text{avg},2}$. The other curves show results for the drives found using optimal control. The idealized PCAA results (red crosses) are obtained using the Schrödinger equation with retained long-range couplings, but without decay, dephasing, and inhomogeneity with the pulse parametrization (8). They lie very close to the line $P_1 - P_0 = N$. The results using optimal control for PCAA (blue circles) and Rydberg atoms (green triangles) are obtained with the master equation or the quantum trajectory method with the parametrization (7). In all cases except the idealized PCAA, the inhomogeneity is modeled by averaging over a number of realizations, and the error bars show the standard deviation of this averaging. The number of inhomogeneity realizations is chosen to be 100, except for CW PCAA with $N = 16$, where only 15 realizations are used, because each one of them needs a slow global optimization [55,56].

Besides the inhomogeneity in the system, the other important imperfection is the finite $T_\phi = 15\,\text{ns}$, which is not much larger than the chosen amplification time of 6.5 ns. To quantify the influence of inhomogeneity in isolation from the other imperfections, pulse shapes were also optimized for a homogeneous ensemble with $N = 16$. After 44 iterations, each with 408 time steps for speed, starting from a pulse shape optimized by the Schrödinger equation, $P_1 - P_0 = 6.2$ was obtained, which is the same as the result for the inhomogeneous ensemble within the uncertainty. For the homogeneous ensemble, optimization with the master equation is more important. Using a pulse shape taken directly from the Schrödinger equation optimization and evaluating it with the master equation gives $P_1 - P_0 = 4.3$, which is smaller than even the result obtained for the inhomogeneous ensemble with the same procedure. This suggests that optimizing the pulse shapes with the included inhomogeneity also makes them more robust against the decoherence, even when the latter is not explicitly included in the model.

Setting T_1 and T_ϕ to be infinite by using the Schrödinger equation result for $N = 16$ gives $P_1 - P_0 = 8.0 \pm 1.0$ with inhomogeneity or $P_1 - P_0 = 14.4$ without inhomogeneity. The latter result is limited by the pulse shape constraints. Relaxing the constraints by using the pulse parametrization (8), the theoretical upper bound $P_1 - P_0 = N$ is closely approached. This is shown by the red crosses in Fig. 3. Even in this more

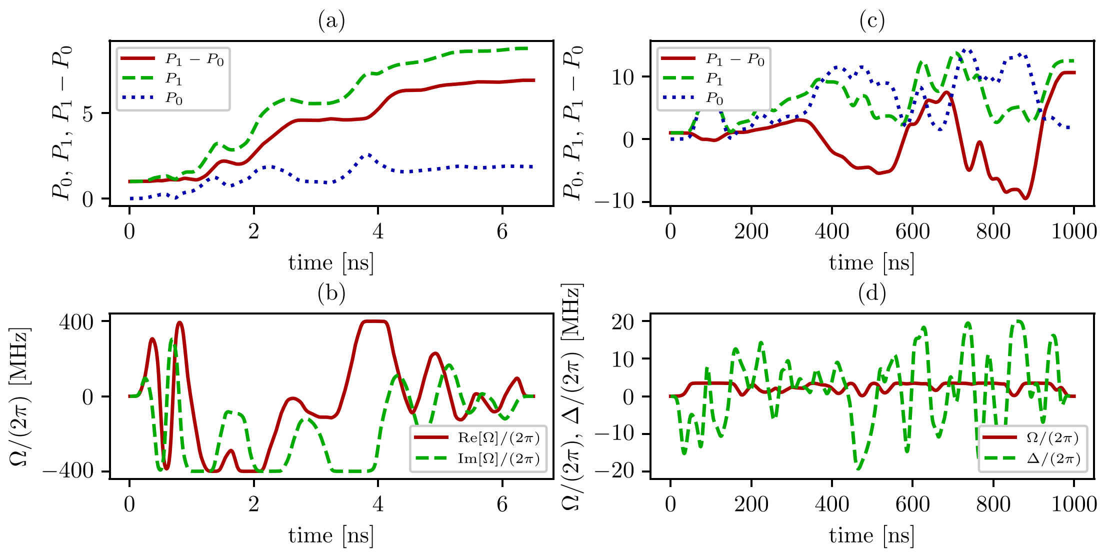

FIG. 4. (a) Populations as functions of time for one inhomogeneity realization of $N = 16$ persistent-current artificial atoms as spins. (b) Pulse shapes that drive the dynamics in panel (a). The pulse shapes are parametrized such that the extremal values of Re$[\Omega]/(2\pi)$ and Im$[\Omega]/(2\pi)$ [cf. Eq. (7)] are at ± 400 MHz, and the filtering bandwidth is $1/\sigma = 4$ GHz. (c) Average populations as functions of time for 100 inhomogeneity realizations of $N = 16$ Rydberg atoms as spins. (d) Pulse shapes that drive the dynamics in panel (c). The Rabi frequency $\Omega/(2\pi)$ is real and positive with the maximum value 3.5 MHz. The detuning $\Delta/(2\pi)$ is constrained by the extremal values ± 20 MHz.

idealized setting, optimal control with broadband pulses was found to be necessary, because of the retained long-range couplings and finite-size effects. Optimizing the continuous-wave parametrization (9) and the amplification time (up to 800 ns) for $N = 16$ gives only $P_1 - P_0 = 6.9$.

Using the pulse with a linear ramp of Δ inspired by the adiabatic state preparation [39] gives $P_1 - P_0 = 10.0$ for the optimized [55,56] minimum and maximum $|\Delta|/(2\pi) \approx 9.7 \times 40$ MHz and Rabi frequency $\Omega/(2\pi) \approx 1.2 \times 40$ MHz. This is the only case where the Δ-ramp pulse improves on the continuous-wave parametrization (9). With realistic dephasing and inhomogeneity, both for the persistent-current artificial atoms and the Rydberg atoms, the Δ-ramp pulse gives worse results. A discussion of these pulses can also be found at the end of Appendix D.

The dynamics in time of the spin populations with the optimal control pulses is shown in Fig. 4(a), and the corresponding pulse shapes are shown in Fig. 4(b). The population difference $P_1 - P_0$ does not necessarily increase monotonically in contrast to the weak continuous-wave spin amplification [17–19].

The above results for the persistent-current artificial atoms were using the delocalized single excitation given by Eq. (4). We have also checked the performance with the localized excitation $|\psi_1\rangle = \hat{\sigma}_{+,j=1}|\psi_0\rangle$, where $j = 1$ is the corner spin [19]. For $N = 16$ and using the same optimization procedure as for the state (4), $P_1 - P_0 = 7.0 \pm 1.1$ is obtained. This is larger than $P_1 - P_0 = 5.7 \pm 0.9$ obtained for the state (4) and suggests that amplifying delocalized states is more challenging.

The results for the Rydberg atoms are shown by green triangles in Fig. 3. The optimization for $N = 16$ is done in the same way as for the persistent-current artificial atoms. First, the pulse shapes are found using the Schrödinger equation that includes the inhomogeneity [cf. Fig. 4(d)], and then they are evaluated using the quantum trajectory method with $T_1 = 175$ µs and $T_\phi = 20$ µs [cf. Fig. 4(c)], resulting in $P_1 - P_0 = 10.6 \pm 0.4$ for $N = 16$. This value for $P_1 - P_0$ is more limited by the pulse shape constraints compared to the persistent-current artificial atoms.

The optimal control result for the Rydberg atoms can be compared to the optimized [55,56] continuous-wave parametrization (9) [within the bounds $\Omega_l/(2\pi) \in [0.1, 2.4] \times 1$ MHz, $\Delta_{\mathrm{avg},l}/(2\pi) \in [-5, 5] \times 1$ MHz to account for the changed frequency scales] that gives $P_1 - P_0 = 6.5 \pm 0.7$ for the amplification time of 1.1 µs (up to 5 µs was considered). Using a pulse with a linear ramp of Δ inspired by the adiabatic state preparation [39] gives a worse $P_1 - P_0 = 5.6 \pm 0.1$ for the optimized [55,56] minimum and maximum $|\Delta|/(2\pi) \approx 7.4$ MHz, Rabi frequency $\Omega/(2\pi) \approx 0.5$ MHz, and ramping time of 20 µs, where the maximum $P_1 - P_0$ is achieved for the evolution time 6.7 µs.

IV. DISCUSSION AND CONCLUSION

Spin amplification is both useful in itself for quantum sensing or measurement, and as a step on the way to the universal quantum computation with a global driving field. For the quantum measurement of a single spin excitation with a global drive, spin amplification could be used before the global excitation is measured. In the above, we have considered persistent-current artificial atoms operated away from the degeneracy point as spins. In this case, the two spin states are associated with different magnetic fields that can be distinguished by a magnetometer. A superconducting quantum interference device fabricated on the same chip such that it encloses the entire ensemble could be used as such a magnetometer [57]. For the Rydberg atoms, one of the detection mechanisms relies on the selective trapping of the two spin states: atoms in the ground states are trapped and imaged, while the atoms in the excited (Rydberg) states are repelled from the trapping sites [2,3].

The single excitation that is amplified could be a result of an absorption of a single photon. In this case, spin amplification can be viewed as having the same function as the internal dynamics of the single-photon avalanche detectors [23,58]. This can enable photodetectors in the frequency ranges where the technology is less developed. Superconducting artificial atoms as spins could detect the microwave photons, and Rydberg atoms could detect the terahertz photons [23].

Our results show that optimal control can significantly reduce the time needed for the amplification. For the Rydberg atoms, Ref. [23] found that amplification in a one-dimensional (1D) array of 11 spins could be done in 25 μs using weak continuous-wave drives, while we show that amplification in a 2D array of 16 spins could be done in 1 μs using optimal control, either a simpler form that uses two optimized frequency components or with a broadband pulse shape that achieves better amplification. Since the dephasing time T_ϕ of the Rydberg levels is around 20 μs [3], much faster amplification time using optimal control is the key improvement that makes spin amplification implementable using these spins. For the persistent-current artificial atoms, our calculations show that amplification time of 6.5 ns is possible using optimal control, which also makes it shorter than $T_\phi = 15$ ns, providing another example that faster operations using optimal control are essential for spin amplification in realistic spins.

Universal quantum computation with globally driven spin ensembles is also possible [13,14,16,21,22]. The techniques that we have developed for the analysis of spin amplification could be used to better understand which other operations can be performed with such setups even in the presence of imperfections.

It is possible to have ensembles with much larger numbers of spins in the experimental setups of Refs. [2,3,33] than we have considered. To find pulse shapes for such ensembles theoretically, the direct simulation of the exponentially large Hilbert space is impossible. Alternative approaches, such as the matrix-product states [2,3,59] or semiclassical methods [59], will be required. Experimentally, the pulses could also be found by optimizing the setup directly [60]. The latter approach will be required to optimize the pulses for every static inhomogeneity realization, as we have assumed for the persistent-current artificial atoms. For the Rydberg atoms, where the inhomogeneity is significantly smaller, the pulse shapes found theoretically can be applied to any inhomogeneity realization, and thus it should be possible to use them as a starting point for implementing spin amplification in the experimental setups.

To conclude, our calculations show that spin amplification is possible in noisy spin ensembles consisting of superconducting persistent-current artificial atoms or Rydberg atoms. This is done by employing optimal control techniques to find classical drive pulse shapes. Therefore, the time of the spin amplification is significantly shortened compared to the previous protocols that use weak continuous-wave drives.

ACKNOWLEDGMENTS

We thank Kosuke Kakuyanagi for useful discussions. We are grateful for the help and support provided by the Scientific Computing and Data Analysis section of Core Facilities at OIST.

DATA AVAILABILITY

The data that support the findings of this study were generated by numerical simulations. The data and the source code used to generate the data are publicly available [61].

APPENDIX A: PERSISTENT-CURRENT ARTIFICIAL ATOMS

In this Appendix, we show how the spin Hamiltonian (2) can be derived from the circuit quantization of the persistent-current artificial atoms [27]. We need to include the self-inductance terms in the artificial atom Hamiltonian [62–65], because they significantly modify the transition frequencies and are needed to introduce the couplings that are caused by the mutual inductance. The inductance matrix **L** that combines both the self-inductances (diagonal elements) and the mutual inductances (off-diagonal elements) is calculated using a version of FASTHENRY [66] that includes the kinetic inductance due to superconductivity [67].

For the calculation of the kinetic inductance, we set the London penetration depth $\lambda = 0.2$ μm as an order-of-magnitude estimate, in line with the measurements of the aluminum thin films [68]. The loops of the persistent-current artificial atoms are set to be squares with the design value for the side length equal to 3 μm, but due to finite accuracy of the electron-beam lithography, these lengths have an error, which we set to be 3 nm [69]. The centers of the artificial atoms are assumed to be fixed, and it is thus only their loop areas that are changing between the inhomogeneity realizations. For every such realization, a different input file to FASTHENRY is generated, with the side lengths sampled from a normal distribution with the average value 3 μm and standard deviation 3 nm. The other parameters are given in the caption of Fig. 2. We get the self-inductance $L = 37.45 \pm 0.03$ pH and the mutual inductance of the nearest neighbors $M = -0.2187 \pm 0.0006$ pH. The factors f_j in the Hamiltonian (2) are equal to the ratio of the actual area of the superconducting loop to the design value, and Ω is the time-dependent Rabi frequency that assumes the coupling to a loop with the design value of the area.

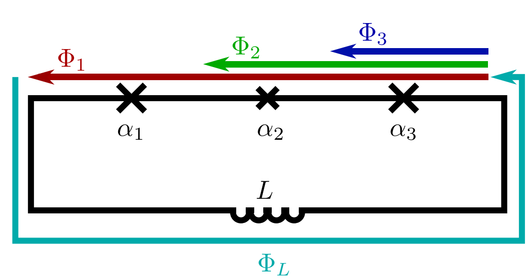

FIG. 5. Flux variable definitions. The integration contours that correspond to the flux variables are displaced out of the circuit for clarity, since some of them overlap.

Before the Hamiltonian can be found, a classical Lagrangian $\mathcal{L}_j$ for the persistent-current artificial atom j is determined from the flux variables shown in Fig. 5. The index j is omitted on the flux variables for brevity. The fluxes are time integrals of voltages $\Phi_C(t) = \int_{-\infty}^{t} V_C(t')\mathrm{d}t'$, and the voltages are electric field line integrals $V_C = \int_C \vec{E}\cdot \mathrm{d}\vec{l}$ [70,71] along the different contours C that are segments of the loop, as shown in Fig. 5. There is gauge freedom [70,71] in the sense that different choices of the contours C are possible [63–65], but they all lead to the same quantum energy levels. The total inductive energy in the ensemble is $\vec{\Phi}_L^{\mathrm{T}}\mathbf{L}^{-1}\vec{\Phi}_L$ [71], where $\vec{\Phi}_L$ is a vector with N elements for the fluxes that correspond to the linear inductances in each artificial atom and $\mathbf{L}^{-1}$ is the inverse of the inductance matrix. We include the diagonal terms of this expression that are proportional to $(\mathbf{L}^{-1})_{jj}$ in the potential energies of each artificial atom. The off-diagonal terms are subsequently projected onto the eigenstates to give the couplings between the artificial atoms.

We have $\mathcal{L}_j = T_j - U_j$, where the kinetic energy is

$$T_j = \frac{\alpha_1 C_\mathrm{J}}{2}(\dot{\Phi}_1 - \dot{\Phi}_2)^2 + \frac{\alpha_2 C_\mathrm{J}}{2}(\dot{\Phi}_2 - \dot{\Phi}_3)^2 + \frac{\alpha_3 C_\mathrm{J}}{2}\dot{\Phi}_3^2, \tag{A1}$$

the potential energy is

$$U_j = (\mathbf{L}^{-1})_{jj}\frac{\Phi_L^2}{2} - \alpha_1 E_\mathrm{J}\cos\left(\frac{2\pi}{\Phi_0}(\Phi_1 - \Phi_2)\right) - \alpha_2 E_\mathrm{J}\cos\left(\frac{2\pi}{\Phi_0}(\Phi_2 - \Phi_3)\right) - \alpha_3 E_\mathrm{J}\cos\left(\frac{2\pi}{\Phi_0}\Phi_3\right), \tag{A2}$$

and $\Phi_0 = h/(2e) \approx 2.068 \times 10^{-15}$ Wb is the magnetic flux quantum. The Josephson-junction energies E_J and capacitances C_J are proportional to the Josephson-junction area and are scaled by the factors α_l. In the ideal case, $\alpha_1 = \alpha_3 = 1$ and $\alpha_2 = \alpha = 0.7$, but due to fabrication imperfections the actual values deviate from the ideal ones. For the calculations with inhomogeneity, the values of α_l are sampled from a normal distribution with the average value μ equal to the ideal one and the standard deviation $\sigma = 0.02$.

The flux variables are not independent, as there is a constraint on the total flux through the loop given by

$$f_j\Phi_\mathrm{ext} = \int_{-\infty}^{t}\oint \vec{E}(t')\cdot \mathrm{d}\vec{l}\mathrm{d}t' = \Phi_1 + \Phi_L, \tag{A3}$$

where Φ_ext is external flux defined to be the value for the design loop area, and the scale factors f_j [the same as in Hamiltonian (2)] are used to model the loop area inhomogeneity. This is the dominant contribution to the standard deviation of Δ_j in Hamiltonian (2), and it is an order of magnitude larger than the contribution due to the standard deviation of the factors α_l.

The flux variable Φ_1 can be eliminated using the constraint above. Assuming external flux that is constant in time, $\dot{\Phi}_\mathrm{ext} = 0$, the kinetic energy is

$$T_j = \frac{\alpha_1 C_\mathrm{J}}{2}(\dot{\Phi}_L + \dot{\Phi}_2)^2 + \frac{\alpha_2 C_\mathrm{J}}{2}(\dot{\Phi}_2 - \dot{\Phi}_3)^2 + \frac{\alpha_3 C_\mathrm{J}}{2}\dot{\Phi}_3^2, \tag{A4}$$

and the potential energy is

$$U_j = (\mathbf{L}^{-1})_{jj}\frac{\Phi_L^2}{2} - \alpha_1 E_\mathrm{J}\cos\left(\frac{2\pi}{\Phi_0}(f_j\Phi_\mathrm{ext} - \Phi_L - \Phi_2)\right) - \alpha_2 E_\mathrm{J}\cos\left(\frac{2\pi}{\Phi_0}(\Phi_2 - \Phi_3)\right) - \alpha_3 E_\mathrm{J}\cos\left(\frac{2\pi}{\Phi_0}\Phi_3\right). \tag{A5}$$

The kinetic energy can be written in terms of the capacitance matrix

$$\mathbf{C} = C_\mathrm{J}\begin{pmatrix}\alpha_1 + \alpha_2 & -\alpha_2 & \alpha_1 \\ -\alpha_2 & \alpha_2 + \alpha_3 & 0 \\ \alpha_1 & 0 & \alpha_1\end{pmatrix} \tag{A6}$$

as $T_j = (1/2)\dot{\vec{\Phi}}^\mathrm{T}\mathbf{C}\dot{\vec{\Phi}}$, where $\vec{\Phi}^\mathrm{T} = (\Phi_2, \Phi_3, \Phi_L)$ is the transpose of $\vec{\Phi}$.

The next step is to perform the Legendre transformation and thereby find the classical Hamiltonian. For the Legendre transformation, the vector of the canonical momenta is determined as

$$\vec{Q} = \frac{\partial \mathcal{L}_j}{\partial \dot{\vec{\Phi}}} = \mathbf{C}\dot{\vec{\Phi}}. \tag{A7}$$

The classical Hamiltonian is then

$$H_j = \vec{Q}^\mathrm{T}\dot{\vec{\Phi}} - \mathcal{L}_j = 2T_j - \mathcal{L}_j = T_j + U_j, \tag{A8}$$

where the kinetic energy written in terms of the canonical momenta is $T_j = (1/2)\vec{Q}^\mathrm{T}\mathbf{C}^{-1}\vec{Q}$.

Performing the canonical quantization, the Poisson bracket $\{\Phi_l, Q_m\} = \delta_{l,m}$ is replaced with the commutator $[\hat{\Phi}_l, \hat{Q}_m] = i\hbar\delta_{l,m}$. Defining the dimensionless external flux $f = \Phi_\mathrm{ext}/\Phi_0$ and operators

$$\hat{n}_l = \frac{1}{2e}\hat{Q}_l, \quad \hat{\varphi}_l = \frac{2\pi}{\Phi_0}\hat{\Phi}_l, \tag{A9}$$

with the commutator $[\hat{\varphi}_l, \hat{n}_m] = i\delta_{l,m}$, the kinetic energy can be written as $\hat{T}_j = 4E_C\vec{n}^\mathrm{T}\mathbf{C}^{-1}\vec{n}$ with $E_C = e^2/(2C_\mathrm{J})$. The Hamiltonian is

$$\hat{H}_j = \hat{T}_j + \tfrac{1}{2}E_L\hat{\varphi}_L^2 - \alpha_1 E_\mathrm{J}\cos(2\pi f_j f - \hat{\varphi}_L - \hat{\varphi}_2) - \alpha_2 E_\mathrm{J}\cos(\hat{\varphi}_2 - \hat{\varphi}_3) - \alpha_3 E_\mathrm{J}\cos(\hat{\varphi}_3), \tag{A10}$$

where $E_L = (\mathbf{L}^{-1})_{jj}(\Phi_0/(2\pi))^2$.

In the limit $L \to 0$ ($E_L \to \infty$), the constraint $\hat{\varphi}_L = 0$ is imposed. Replacing $\hat{\varphi}_2 \to \hat{\varphi}_2 - \hat{\varphi}_1$ and $\hat{\varphi}_3 \to -\hat{\varphi}_1$, and using the ideal $\alpha_1 = \alpha_3 = 1$, $\alpha_2 = \alpha$, and $f_j = 1$, the Hamiltonian reduces to the one considered in Ref. [27]:

$$\hat{H}_{j,0} = T_{j,0} - (E_\mathrm{J}\cos(\hat{\varphi}_1) + E_\mathrm{J}\cos(\hat{\varphi}_2) + \alpha E_\mathrm{J}\cos(2\pi f + \hat{\varphi}_1 - \hat{\varphi}_2)). \tag{A11}$$

The end result of the Hamiltonian diagonalization can be written as $\hat{H}_j = \sum_{\nu=0}^{\infty} E_{\nu,j}|\nu_j\rangle\langle\nu_j|$ in terms of the eigenenergies $E_{\nu,j}$ and the eigenvectors $|\nu_j\rangle$. For a finite L, there is a significant difference in the spectrum between the Hamiltonians $\hat{H}_{j,0}$ and $\hat{H}_j$, as shown in Fig. 6. Our parameters approximately correspond to $E_L/E_\mathrm{J} = 14.5$ (ignoring the mutual inductance), and for this value the Hamiltonian (A10) gives $(E_{1,j} - E_{0,j})/h = 7.9$ GHz, while the Hamiltonian (A11) gives $(E_{1,j} - E_{0,j})/h = 8.4$ GHz.

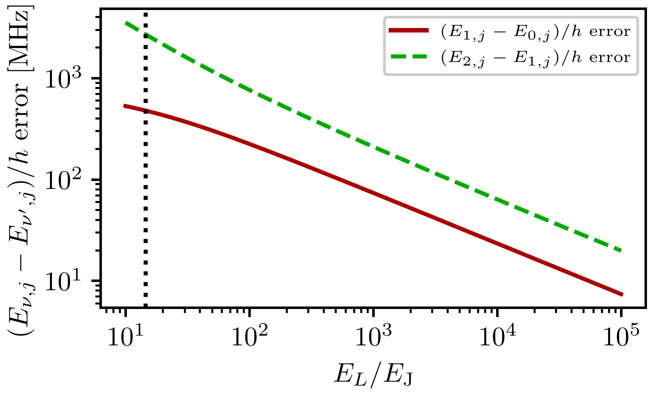

FIG. 6. The error in calculating the transition frequencies $(E_{1,j} - E_{0,j})/h$ and $(E_{2,j} - E_{1,j})/h$ for a persistent-current artificial atom j using the zero-self-inductance Hamiltonian (A11) compared to the Hamiltonian (A10) that accounts for the finite self-inductance. The error is plotted as a function of the ratio of the inductive energy E_L and Josephson energy E_J. For the Hamiltonian (A10), the ideal values $\alpha_1 = \alpha_3 = 1$, $\alpha_2 = \alpha$, and $f_j = 1$ are used. The bias flux is $f = \Phi_\mathrm{ext}/\Phi_0 = 0.5034$ in both cases. Other parameters are stated in the caption of Fig. 2, but the Josephson-junction area error is not included. Assuming that the artificial atom is isolated, i.e., the inductance matrix $\mathbf{L}$ has only one element $L = 37.4\,\mathrm{pH}$, we have $E_L/E_\mathrm{J} = 14.5$, which is shown by the black dotted vertical line.

For the case of finite but small L that we consider, the term $(1/2)E_L\hat{\varphi}_L^2$ is dominant in the Hamiltonian (A10). To reduce the total number of the basis states required to diagonalize the entire Hamiltonian (A10), a harmonic oscillator basis is chosen where the quadratic part

$$\hat{H}_L = A\hat{n}_L^2 + B\hat{\varphi}_L^2 \tag{A12}$$

is already diagonal. In Eq. (A12), A is proportional to the element of the inverse capacitance matrix $\mathbf{C}^{-1}$ corresponding to $\hat{\varphi}_L$, and $B = (1/2)E_L$. The operators are written as $\hat{\varphi}_L = \frac{1}{C_L}\frac{1}{\sqrt{2}}(\hat{a} + \hat{a}^\dagger)$ and $\hat{n}_L = -iC_L\frac{1}{\sqrt{2}}(\hat{a} - \hat{a}^\dagger)$, where the creation operator $\hat{a}^\dagger$ and the annihilation operator $\hat{a}$ are defined by their actions on the Fock states $|n_L\rangle$. We have $\hat{a}^\dagger|n_L\rangle = \sqrt{n_L + 1}|n_L + 1\rangle$ and $\hat{a}|n_L\rangle = \sqrt{n_L}|n_L - 1\rangle$. The commutator $[\hat{\varphi}_L, \hat{n}_L] = i$ is satisfied for any choice of the constant C_L, but to diagonalize Eq. (A12), a particular $C_L = (B/A)^{1/4}$ is chosen, resulting in $\hat{H}_L = 2\sqrt{AB}(\hat{a}^\dagger\hat{a} + \frac{1}{2})$.

For the representation of the Josephson-junction operators in phases $\hat{\varphi}_2$ and $\hat{\varphi}_3$, and the corresponding charge numbers $\hat{n}_2$ and $\hat{n}_3$ in Eq. (A10), the charge basis is used. In this basis, the eigenstates are $|n_l\rangle$, where $l = 2, 3$, and the operators can be written as $\hat{n}_l = \sum_{n_l=-\infty}^{\infty} n_l|n_l\rangle\langle n_l|$ and $e^{-i\hat{\varphi}_l} = \sum_{n_l=-\infty}^{\infty}|n_l\rangle\langle n_l - 1|$. In the harmonic oscillator basis, $e^{-i\hat{\varphi}_L}$ is computed using matrix exponentiation. The Hilbert spaces of the Josephson junctions are truncated to 21 charge states each, and the harmonic oscillator basis to 8 Fock states.

For the numerical diagonalization of Eq. (A10), the matrix exponentials are decomposed using tensor products. For example, the expression $e^{i\hat{\varphi}_2 - i\hat{\varphi}_3}$ in Eq. (A10) is actually

$$\begin{aligned}&\exp(i\hat{\varphi}_2 \otimes \hat{I}_3 \otimes \hat{I}_L - i\hat{I}_2 \otimes \hat{\varphi}_3 \otimes \hat{I}_L)\\ &= \exp(i\hat{\varphi}_2) \otimes \exp(-i\hat{\varphi}_3) \otimes \hat{I}_L,\end{aligned} \tag{A13}$$

where $\hat{I}_2$, $\hat{I}_3$, and $\hat{I}_L$ are the identity operators on the respective Hilbert spaces. In Eq. (A13), we have used the fact that $e^{\hat{A}+\hat{B}} = e^{\hat{A}}e^{\hat{B}}$ for commuting matrices $\hat{A}$ and $\hat{B}$, and that

$$\exp(\hat{A} \otimes \hat{I}) = \exp(\hat{A}) \otimes \hat{I}. \tag{A14}$$

Similarly, the other operators in Eq. (A10) are rewritten with the identity operators appearing explicitly. For example, $\hat{Q}_2^2$ becomes $\hat{Q}_2^2 \otimes \hat{I}_3 \otimes \hat{I}_L$. It is the latter types of expressions that are used to assemble the matrix for the numerical diagonalization.

Coupling between the artificial atoms with Hamiltonians $\hat{H}_j$ is due to the off-diagonal elements of the inverse inductance matrix $\mathbf{L}^{-1}$. The Hamiltonian for the entire ensemble can be written as

$$\hat{H}_\mathrm{ensemble} = \sum_j \hat{H}_j + \sum_{\substack{j,k\\ j\neq k}} (\mathbf{L}^{-1})_{jk}\hat{\Phi}_{L,j}\hat{\Phi}_{L,k}. \tag{A15}$$

Making the two-level approximation, the operators $\hat{\Phi}_{L,j}$ are projected onto the subspace spanned by the eigenvectors $|0_j\rangle$ and $|1_j\rangle$ of $\hat{H}_j$ and hence can be written as the Hermitian 2×2 matrices

$$\hat{\Phi}_{L,j} = \begin{pmatrix} \langle 0_j|\hat{\Phi}_{L,j}|0_j\rangle & \langle 0_j|\hat{\Phi}_{L,j}|1_j\rangle \\ \langle 1_j|\hat{\Phi}_{L,j}|0_j\rangle & \langle 1_j|\hat{\Phi}_{L,j}|1_j\rangle \end{pmatrix}. \tag{A16}$$

Such matrices can be decomposed into linear combinations of Pauli matrices and the identity matrix $\hat{I}_j$. Thus,

$$\hat{\Phi}_{L,j} = P_{\hat{I}_j} + P_{\hat{\sigma}_{x,j}}\hat{\sigma}_{x,j} + P_{\hat{\sigma}_{y,j}}\hat{\sigma}_{y,j} + P_{\hat{\sigma}_{z,j}}\hat{\sigma}_{z,j}, \tag{A17}$$

where $P_{\hat{O}_j}$ for $\hat{O}_j \in \{\hat{I}_j, \hat{\sigma}_{x,j}, \hat{\sigma}_{y,j}, \hat{\sigma}_{z,j}\}$ are real coefficients found via the Hilbert-Schmidt inner product

$$P_{\hat{O}_j} = \tfrac{1}{2}\mathrm{tr}[\hat{\Phi}_{L,j}\hat{O}_j]. \tag{A18}$$

The eigenvectors are defined up to a phase, and the relative phases of the lowest-energy states $|0_j\rangle$ and $|1_j\rangle$ are chosen such that $\langle 0_j|\hat{\Phi}_{L,j}|1_j\rangle$ is real. This results in $P_{\hat{\sigma}_{y,j}} = 0$, but we still keep it in the expressions for generality.

Inserting Eq. (A17) into Eq. (A15), applying the rotating-wave approximation, and removing constants, we get

$$\begin{aligned}\hat{H}_\mathrm{ensemble} = \hbar\sum_j \frac{\omega_j}{2}\hat{\sigma}_{z,j} + \hbar\sum_{\substack{j,k\\ j\neq k}} J_{z,jk}\hat{\sigma}_{z,j}\hat{\sigma}_{z,k}\\ + \hbar\sum_{\substack{j,k\\ j\neq k}} J_{\pm,jk}\hat{\sigma}_{+,j}\hat{\sigma}_{-,k},\end{aligned} \tag{A19}$$

with

$$\omega_j = \frac{E_{1,j} - E_{0,j}}{\hbar} + 4\sum_{\substack{k\\ k\neq j}} \frac{(\mathbf{L}^{-1})_{jk}}{\hbar}P_{\hat{\sigma}_{z,j}}P_{\hat{I}_k}, \tag{A20}$$

$$J_{z,jk} = \frac{(\mathbf{L}^{-1})_{jk}}{\hbar}P_{\hat{\sigma}_{z,j}}P_{\hat{\sigma}_{z,k}}, \tag{A21}$$

$$J_{\pm,jk} = 2\frac{(\mathbf{L}^{-1})_{jk}}{\hbar}\big(P_{\hat{\sigma}_{x,j}} - iP_{\hat{\sigma}_{y,j}}\big)\big(P_{\hat{\sigma}_{x,k}} + iP_{\hat{\sigma}_{y,k}}\big). \tag{A22}$$

The coupling $J_{\pm,jk}$ is real because of $P_{\hat{\sigma}_{y,j}} = 0$. Adding the driving terms and going into the rotating frame with respect to $\hat{H}_0 = (\hbar\omega_\mathrm{d}/2)\sum_j \hat{\sigma}_{z,j}$ results in the Hamiltonian (2) of the main text. Note that Eq. (A20) shows that even without fabrication imperfections, there is a small inhomogeneous broadening in the renormalized spin frequencies due to the fact that spins experience different sums of mutual inductances between them and the neighbors.

APPENDIX B: REDUCED-STORAGE OPERATORS

In this Appendix, we show how the action of the quantum mechanical operators and superoperators can be calculated with reduced storage requirements. The state vectors ψ are propagated in time using the Schrödinger equation

$$\dot{\psi} = -\frac{i}{\hbar}\hat{H}\psi, \tag{B1}$$

where the Hamiltonian $\hat{H}$ is given by either Eq. (1) or (2), and the ket notation on the state vectors is omitted. The density matrices ρ are propagated in time using the Markovian zero-temperature master equation

$$\dot{\rho} = -\frac{i}{\hbar}[\hat{H},\rho] + \gamma\sum_j \mathcal{D}[\hat{\sigma}_{-,j}]\rho + \gamma_{\mathrm{d}}\sum_j \mathcal{D}[\hat{\sigma}_{z,j}]\rho, \tag{B2}$$

where $\mathcal{D}[\hat{o}]\rho = \frac{1}{2}(2\hat{o}\rho\hat{o}^\dagger - \rho\hat{o}^\dagger\hat{o} - \hat{o}^\dagger\hat{o}\rho)$.

For an ensemble of two-level systems, there is a direct mapping between binary numbers and basis states. The zero-excitation state ψ_0 [Eq. (3)] is mapped to the binary number 0. A basis state $\hat{\sigma}_{+,j}\hat{\sigma}_{+,k}\psi_0$ that has spins j and k up and all other spins down is mapped to the binary number where bits j and k are set (equal to 1), and all the other bits are reset (equal to 0). Interpreted as an integer, this number has value $2^j + 2^k$ (if j and k are zero-based indices), but exponentiation is not needed to calculate it—only bitwise operations that directly set the corresponding bits. The amplitudes of the state vector ψ are stored in an array with the positions corresponding to the binary numbers obtained by the above mapping. For the density matrix ρ, both the row and the column of an element are determined by this mapping. Thus, given a basis state specification (i.e., which spins are up and which are down), it allows to quickly determine the position of the corresponding state vector amplitude or density matrix element in the stored arrays. This leads to an efficient calculation of the action of operators both in the Schrödinger equation (B1) and the master equation (B2).

The commutator term on the right-hand side of master equation (B2) can be written as

$$-\frac{i}{\hbar}[\hat{H},\rho] = -\frac{i}{\hbar}\hat{H}\rho + \left(-\frac{i}{\hbar}\hat{H}\rho\right)^\dagger, \tag{B3}$$

where we have used the fact $\hat{H}$ and ρ are Hermitian, i.e., $\hat{H}^\dagger = \hat{H}$ and $\rho^\dagger = \rho$. Writing the commutator term like this shows that only $-\frac{i}{\hbar}\hat{H}\rho$ needs to be calculated by applying $-\frac{i}{\hbar}\hat{H}$ to each column of ρ, just like in a Schrödinger equation (B1), and then the adjoint of the resulting matrix can be added to itself to obtain $-\frac{i}{\hbar}[\hat{H},\rho]$. Hence, we first need to be able to calculate the action of $\hat{H}$ on a state vector ψ.

The operators $-\sum_j \Delta\hat{n}_j$, $\sum_{j\neq k} J_{z,jk}\hat{n}_j\hat{n}_k$ in the Hamiltonian (1) and $-\sum_j \frac{\Delta_j}{2}\hat{\sigma}_{z,j}$, $\sum_{j\neq k} J_{z,jk}\hat{\sigma}_{z,j}\hat{\sigma}_{z,k}$ in the Hamiltonian (2) are diagonal. Therefore, their storage requirements are the same as for the state vector ψ itself. Even though the action of these operators could be calculated on the fly, we find that for all of them except $-\sum_j \Delta\hat{n}_j$, storing the diagonal of the matrix and multiplying it onto ψ is faster. The operator $-\sum_j \Delta\hat{n}_j$ has all the detunings equal and can be calculated efficiently without any storage. It will be explained below, as the same approach is used for the homogeneous part of the operator $-\sum_j \frac{\Delta_j}{2}\hat{\sigma}_{z,j}$. In principle, however, action of all of these operators could be calculated in a completely matrix-free way by adapting the code below to immediately multiply each element of ψ with a corresponding element of the operator diagonal instead of storing it.

TABLE I. Logical and bitwise operators used in the pseudocode examples.

Operator	Description
`<<`	Bitwise shift
`&`	Bitwise AND
`|`	Bitwise OR
`^`	Bitwise XOR
`~`	Bitwise NOT
`&&`	Logical AND
`||`	Logical OR
`!`	Logical NOT

We will explain both this and the other computations in terms of the pseudocode where the bitwise and logical operators follow the conventions of C and C++ languages. The operators are listed in Table I. The loops in the pseudocode are written in terms of zero-based indices. For example, `n` is an index of the basis for which it holds that $0 \leqslant$ `n` $\leqslant 2^N - 1$, and `j`, `k` are indices of the spins for which it holds that $0 \leqslant$ `j`, `k` $\leqslant N - 1$. The basis size is written compactly using the bitwise shift operator as `1 << N`, which is equal to 2^N. The variables are set using =, so that `n = n + 1` means that 1 is added to `n`.

Assume that the detunings Δ_j are stored in an array `Delta`, with the elements `Delta[j]` $= \Delta_j$. To calculate the diagonal `d` (an array of size 2^N with elements `d[n]`) of the operator $-\sum_j \frac{\Delta_j}{2}\hat{\sigma}_{z,j}$, the following pseudocode could be used:

```
for n = 0 to (1 << N) − 1
    d[n] = 0
    for j = 0 to N − 1
        if n & (1 << j) then
            d[n] = d[n] − 0.5*Delta[j]
        else
            d[n] = d[n] + 0.5*Delta[j]
        end if
    end for
end for
```

In the above, the diagonal element `d[n]` is initialized with the value zero. Then, iterating over the spin index `j`, the expression `n & (1 << j)` is used to test whether bit `j` is set in the basis state index `n`. Depending on the result of this test, `0.5*Delta[j]` is either subtracted from or added to `d[n]`.

To add the contribution of the term $\sum_{j\neq k} J_{z,jk}\hat{\sigma}_{z,j}\hat{\sigma}_{z,k}$ to the diagonal `d`, assume that the shifts $J_{z,jk}$ are stored in a matrix `J_z` with the elements `J_z[j][k]` $= J_{z,jk}$ if $j \neq k$ and

J_z[j][k] $= 0$ if $j = k$. Then, the following pseudocode could be used:

```
for n = 0 to (1 << N) − 1
    for j = 0 to N − 1
        for k = 0 to N − 1
            nj = n & (1 << j)
            nk = n & (1 << k)
            if (nj && nk) || (!nj && !nk)
            then
               d[n] = d[n] + J_z[j][k]
            else
               d[n] = d[n] − J_z[j][k]
            end if
        end for
    end for
end for
```

In the above, `(nj && nk) || (!nj && !nk)` evaluates to logical TRUE if both bits `j` and `k` are set or both bits are reset. In this case, `J_z[j][k]` is added to `d[n]`. Otherwise, `J_z[j][k]` is subtracted. The above code can be adjusted to realize the operator $\sum_{j\neq k} J_{z,jk}\hat{n}_j\hat{n}_k$ instead by using

```
            if (nj && nk)
            then
               d[n] = d[n] + J_z[j][k]
            end if
```

in the inner loop, since $\hat{n}_j\hat{n}_k$ only gives a contribution when both spins are excited.

In the Hamiltonian (2), the detunings are written as $\Delta_j = \Delta_{\rm avg} + \omega_{01,\rm avg} - \omega_{01,j}$, where the detuning from the average frequency $\Delta_{\rm avg}$ is also being optimized together with the pulse parameters a_p and b_p. Thus, to avoid recomputation of the diagonal `d` for every new value of $\Delta_{\rm avg}$, we store only $\omega_{01,\rm avg} - \omega_{01,j}$ in the array `Delta`. The operator $-\frac{\Delta_{\rm avg}}{2}\sum_j \hat{\sigma}_{z,j}$ is applied separately without additional storage. This is accomplished with the instruction `popcount` (population count) that counts the number of set bits in a binary number. Assuming that the variable `Delta_avg` holds the value of $\Delta_{\rm avg}$, the state vector ψ is stored in the array `psi`, and the result $r = -\sum_j \frac{\Delta_j}{2}\hat{\sigma}_{z,j}\psi$ is stored in the array `res`, the following pseudocode can be used:

```
for n = 0 to (1 << N) − 1
    s = −0.5*Delta_avg*(2*popcount(n) − N)
    res[n] = (s + d[n])*psi[n]
end for
```

The same approach is used to calculate the action of the operator $-\sum_j \Delta\hat{n}_j$ in the Hamiltonian (1) by changing

```
    s = −Delta*popcount(n)
```

in the code above.

The rest of the operators in the Hamiltonians (1) and (2) are nondiagonal. The driving term $-\Omega\sum_j \hat{\sigma}_{x,j}$ in the Hamiltonian (1) is the simplest to calculate. The action of this operator on the state vector ψ can be implemented with the following pseudocode:

```
for n = 0 to (1 << N) − 1
    sum = 0
    for j = 0 to N − 1
        sum = sum + psi[n ^ (1 << j)]
    end for
    res[n] = res[n] − Omega * sum
end for
```

Applying the XOR operator in a loop over all the spin indices finds the matrix elements between the states that differ by one flipped spin.

The implementation of the driving terms $-\sum_j(\Omega\hat{\sigma}_{+,j} + \Omega^*\hat{\sigma}_{-,j})$ in the Hamiltonian (2) is more involved. It can be done by iterating over the set or reset bits in a binary number. Modern CPUs provide fast instructions to accomplish this. One such instruction is `ctz` (count trailing zeros). Counting the number of the trailing zeros is the same as determining the position of the last set bit. Once the position of the last set bit in a binary number `b` is determined, it can be reset by assigning `b = b & (b − 1)`. This can also be reduced to a single instruction (`blsr`) on modern CPUs. By repeatedly finding and then resetting the last set bit, it is possible to efficiently iterate over all the set bits in the binary number `b`.

The instructions `popcount` and `ctz` can be used in some C/C++ compilers with `__builtin_popcount` (or `std::popcount`) and `__builtin_ctz` (or `std::countr_zero`), respectively. This keeps the code portable, as the compiler will either use the native instructions or generate (slower) code that accomplishes the same operation, depending on the particular CPU.

In the operator $-\sum_j f_j\Omega\hat{\sigma}_{+,j}$, the factors f_j are stored in the array `OmegaFactors`. Then, the action of this operator on the state vector ψ can be implemented with the following pseudocode:

```
for n = 0 to (1 << N) − 1
    sum1 = 0
    b = n
    while b != 0
       sb = ctz(b)
       f = OmegaFactors[sb]
       sum1 = sum1 + f*psi[n & ~(1 << sb)]
       b = b & (b − 1)
    end while
    res[n] = res[n] − Omega * sum1
end for
```

Iterating over the set bits of `n`, the expression `n & ~(1 << sb)` resets the bit at the position `sb` (the currently found set bit in `n`), and the element of `psi` that has this new index is added to `sum1` with a weight `OmegaFactors[sb]`. This sum is multiplied by the variable `Omega` that holds the value of Ω.

Adding the contribution of the operator $-\sum_j f_j\Omega^*\hat{\sigma}_{-,j}$ can be implemented with

```
for n = 0 to (1 << N) − 1
    sum2 = 0
    b = ~n & ((1 << N) − 1)
    while b != 0
       sb = ctz(b)
       f = OmegaFactors[sb]
       sum2 = sum2 + f*psi[n | (1 << sb)]
       b = b & (b − 1)
    end while
```

```
    res[n] = res[n] - conj(Omega) * sum2
end for
```

Instead of iterating over the set bits, this loop iterates over the reset bits, by using the bitwise NOT to transform the binary number `b` compared to the previous loop. When using fixed-size integers for `n` and `b`, the bits above the maximum number of spins are unphysical. However, `~n` has these bits set, and to prevent them from interfering with the subsequent loop that should only iterate over the physically meaningful bits, they are reset by performing the bitwise AND with `(1 << N) - 1`. Inside the loop, the expression `n | (1 << sb)` sets the bit at the position `sb`, and the element of `psi` that has this new index is added to `sum2` with a weight `OmegaFactors[sb]`. This sum is multiplied by `conj(Omega)` that holds the value of Ω^*.

The term $\sum_{j\neq k} J_{\pm,jk}\hat{\sigma}_{+,j}\hat{\sigma}_{-,k}$ in the Hamiltonian (2) can also be implemented by iterating over the set and reset bits. Assuming that the matrix `J_pm` has elements `J_pm[j][k]` $= J_{\pm,jk}$, the following pseudocode can be used:

```
for n = 0 to (1 << N) - 1
    sum = 0
    b = ~n & ((1 << N) - 1)
    while b != 0
        sb = ctz(b)
        c = n
        while c != 0
            sc = ctz(c)
            ns = (n & ~(1 << sc)) | (1 << sb)
            sum = sum + J_pm[sc][sb]*psi[ns]
            c = c & (c - 1)
        end while
        b = b & (b - 1)
    end while
    res[n] = res[n] + sum
end for
```

The code above describes the reduced-storage multiplication of a Hamiltonian $\hat{H}$ onto a state vector ψ. For the master equation (B2), the code needs to operate on each column of the density matrix ρ. Additionally, the reduced-storage action of the dissipators is needed. In the sum of the terms $\gamma\sum_j \mathcal{D}[\hat{\sigma}_{-,j}]\rho + \gamma_{\mathrm{d}}\sum_j \mathcal{D}[\hat{\sigma}_{z,j}]\rho$ in the master equation (B2), only the term $\sum_j \hat{\sigma}_{-,j}\rho\hat{\sigma}_{+,j}$ involves a nondiagonal superoperator acting on ρ. The diagonal terms can be written as

$$\begin{aligned}
&\gamma\sum_j \mathcal{D}[\hat{\sigma}_{-,j}]\rho + \gamma_{\mathrm{d}}\sum_j \mathcal{D}[\hat{\sigma}_{z,j}]\rho - \gamma\sum_j \hat{\sigma}_{-,j}\rho\hat{\sigma}_{+,j}\\
&\quad = -\frac{\gamma}{2}\sum_j(\rho\hat{\sigma}_{11,j} + \hat{\sigma}_{11,j}\rho) - \gamma_{\mathrm{d}}\sum_j(\rho - \hat{\sigma}_{z,j}\rho\hat{\sigma}_{z,j})\\
&\quad = D\odot\rho,
\end{aligned} \tag{B4}$$

where $\odot$ is the elementwise (Hadamard) matrix product, $\hat{\sigma}_{11,j} = \hat{\sigma}_{+,j}\hat{\sigma}_{-,j}$, and we have used that $\hat{\sigma}_{z,j}\hat{\sigma}_{z,j}$ is the identity matrix. Since $\hat{\sigma}_{11,j}$ and $\hat{\sigma}_{z,j}$ are diagonal matrices, we denote their diagonal elements by $\sigma_{11,j,m}$ and $\sigma_{z,j,m}$, respectively. Then, the elements of the matrix D are

$$\begin{aligned}
D_{mn} = &-\frac{\gamma}{2}\sum_j(\hat{\sigma}_{11,j,m} + \hat{\sigma}_{11,j,n})\\
&-\gamma_{\mathrm{d}}\left(N - \left(\sum_j \hat{\sigma}_{z,j,m}\hat{\sigma}_{z,j,n}\right)\right).
\end{aligned} \tag{B5}$$

The nondiagonal superoperator $\sum_j \hat{\sigma}_{-,j}\rho\hat{\sigma}_{+,j}$ can be realized by considering its elements

$$\sum_j \langle m|\hat{\sigma}_{-,j}\rho\hat{\sigma}_{+,j}|n\rangle. \tag{B6}$$

This sum has nonzero terms when for each spin j, both of the basis states $|m\rangle$ and $|n\rangle$ have this spin in state $|0\rangle$. Assuming that the binary number `m` corresponds to the basis state $|m\rangle$, and the binary number `n` corresponds to the basis state $|n\rangle$, the nonzero elements of Eq. (B6) can be found by iterating over the reset bits of the binary number `m | n`. This is equivalent to iterating over the set bits of the binary number `~m & ~n & ((1 << N) - 1)`, where we have used the equivalence

$$\text{NOT}(A \text{ OR } B) = (\text{NOT } A) \text{ AND } (\text{NOT } B) \tag{B7}$$

and masked off the unphysical bits by the bitwise AND with `(1 << N) - 1`.

If we define the variable `gamma` that has the value of γ, the matrix `mul` with the elements `mul[m][n]` $= D_{mn}$, and the matrix `rho` that holds the elements of ρ, the result of the expression $\gamma\sum_j \mathcal{D}[\hat{\sigma}_{-,j}]\rho + \gamma_{\mathrm{d}}\sum_j \mathcal{D}[\hat{\sigma}_{z,j}]\rho$ added to the matrix `res` can be found using the following pseudocode:

```
for n = 0 to (1 << N) - 1
    for m = 0 to n
        sum = 0
        b = ~m & ~n & ((1 << N) - 1)
        while b != 0
            sb = ctz(b)
            ms = m | (1 << sb)
            ns = n | (1 << sb)
            sum = sum + rho[ms][ns]
            b = b & (b - 1)
        end while
        res[m][n] = res[m][n]
                  + gamma*sum
                  + rho[m][n]*mul[m][n]
    end for
end for
```

Since ρ is a Hermitian matrix, its lower triangular part is not stored explicitly. Therefore, the variable `m` (row index) in the above code is iterated over from 0 to `n` [instead of `(1 << N) - 1`]. Omitting the lower triangular part of ρ does not introduce complexity in this code, since both the variables `ms` and `ns` are obtained from `m` and `n`, respectively, by setting the same bit `sb`. This effectively adds the same constant to both. Hence, it holds that `ms` $\leqslant$ `ns`. However, special handling is required for the lower triangular part of ρ when calculating $\hat{H}\rho$. There, ρ gets temporarily uncompressed (filling the lower triangular part) and then compressed again when evaluating Eq. (B3).

APPENDIX C: CALCULATION OF THE GRADIENT

In this Appendix, we describe the calculation of the gradient used in the optimal control. The approach is described in detail in the Appendix of Ref. [47], and here we only discuss the differences. One of them is reducing the storage requirement of the operators and superoperators using Appendix B. Another difference is that both the Schrödinger equation and master equation are used to evolve the initial states and optimize the pulse shapes. For both equations, the detuning $\Delta_{\rm avg}$ from the average spin frequency is also being optimized together with the pulse shape parameters a_p and b_p.

We discuss the master equation case first, as this is what Ref. [47] considered. In the analysis, the density matrix ρ was rewritten as a vector $\vec{\rho}$, so that the master equation (B2) is rewritten as

$$\dot{\vec{\rho}} = \hat{L}\vec{\rho}, \tag{C1}$$

where $\hat{L}$ is a matrix. While such rewriting is useful conceptually, it can make the computations less efficient. Taken literally, it can, for instance, significantly increase the storage requirements. If $\vec{\rho}$ is in the row-major form $(\rho_{l,l'} = (\vec{\rho})_{l2^N+l'})$, then $-\frac{i}{\hbar}[\hat{H},\rho]$ in the master equation (B2) is rewritten as $-\frac{i}{\hbar}(\hat{H}\otimes\hat{I} - \hat{I}\otimes\hat{H}^T)\vec{\rho}$, where $\hat{I}$ is the identity operator, for the corresponding term in the vector master equation (C1). The tensor products $\hat{H}\otimes\hat{I}$ are 2^N copies of the Hamiltonian $\hat{H}$ and therefore have equal or larger storage requirements than the density matrix ρ. Since $\hat{H}$ is usually a sparse matrix, it has lower storage requirements than ρ, and calculating $-\frac{i}{\hbar}[\hat{H},\rho]$ through Eq. (B3) avoids unnecessary storage. Additionally, as Appendix B has shown, neither $\hat{H}$ nor the dissipators $\mathcal{D}$ need to be stored to find their action on ρ, but we store their diagonals as an optimization.

For the master equation, the calculation of the gradient of Eq. (5) reduces to calculation of the gradients

$$\frac{\partial P}{\partial a_p} = \vec{M}^\dagger\frac{\partial\vec{\rho}_{N_t}}{\partial a_p}, \quad \frac{\partial P}{\partial b_p} = \vec{M}^\dagger\frac{\partial\vec{\rho}_{N_t}}{\partial b_p}, \tag{C2}$$

where $\vec{M}$ is the measurement operator $\hat{M}$ in Eq. (5) written as a vector, N_t is the number of time steps, and $\vec{\rho}$ is defined on the discrete times $t_n = n(\Delta t)$ with $\Delta t = t_{\rm f}/N_t$ such that $\vec{\rho}_n = \vec{\rho}(t_n)$. The gradients in Ref. [47] are of the same form as Eq. (C2). The calculations are written in terms of $\hat{L}_{1,n} = \hat{L}(t_n)\Delta t$, $\hat{L}_{2,n} = \hat{L}(t_n + (\Delta t)/2)\Delta t$, $\hat{L}_{3,n} = \hat{L}(t_{n+1})\Delta t$,

$$T_{\rm Re} = -\frac{i}{\hbar}(\Delta t)\big(\tilde{H}_{\rm d,Re}\otimes\hat{I} - \hat{I}\otimes\tilde{H}^T_{\rm d,Re}\big), \tag{C3a}$$

$$T_{\rm Im} = -\frac{i}{\hbar}(\Delta t)\big(\tilde{H}_{\rm d,Im}\otimes\hat{I} - \hat{I}\otimes\tilde{H}^T_{\rm d,Im}\big), \tag{C3b}$$

where $\tilde{H}_{\rm d,Re} = -\hbar\sum_j(\hat{\sigma}_{+,j} + \hat{\sigma}_{-,j})$ and $\tilde{H}_{\rm d,Im} = -i\hbar\sum_j(\hat{\sigma}_{+,j} - \hat{\sigma}_{-,j})$ for the Hamiltonian (2). As an extension, we also calculate $\frac{\partial P}{\partial\Delta_{\rm avg}}$, for which, instead of $T_{\rm Re}$ or $T_{\rm Im}$,

$$T_{\Delta_{\rm avg}} = -\frac{i}{\hbar}(\Delta t)\big(\tilde{H}_{\Delta_{\rm avg}}\otimes\hat{I} - \hat{I}\otimes\tilde{H}^T_{\Delta_{\rm avg}}\big) \tag{C4}$$

is used with $\tilde{H}_{\Delta_{\rm avg}} = -(\hbar/2)\sum_j\hat{\sigma}_{z,j}$. The action of $T_{\rm Re}$, $T_{\rm Im}$, $T_{\Delta_{\rm avg}}$, and $\hat{L}$ on $\vec{\rho}$ is calculated using Eq. (B3) instead of storing the tensor product matrices.

The Schrödinger equation is of the same form as Eq. (C1), with the replacements $\vec{\rho}\to\psi$ and $\hat{L}\to -i\hat{H}/\hbar$. The expression for $P_1 - P_0$ has a slightly different form, however. The spin amplification superoperator $\mathcal{U}$ in Eq. (5) can be written as $\mathcal{U}(\rho) = \hat{U}\rho\hat{U}^\dagger$ with unitary operator $\hat{U}$. Hence, Eq. (5) becomes

$$P_1 - P_0 = \psi_1^\dagger\hat{U}^\dagger\hat{M}\hat{U}\psi_1 - \psi_0^\dagger\hat{U}^\dagger\hat{M}\hat{U}\psi_0. \tag{C5}$$

Instead of Eq. (C2), the gradient is calculated by evaluating

$$\frac{\partial P}{\partial a_p} = 2{\rm Re}\bigg[\psi^\dagger_{N_t}\hat{M}\frac{\partial\psi_{N_t}}{\partial a_p}\bigg], \tag{C6a}$$

$$\frac{\partial P}{\partial b_p} = 2{\rm Re}\bigg[\psi^\dagger_{N_t}\hat{M}\frac{\partial\psi_{N_t}}{\partial b_p}\bigg]. \tag{C6b}$$

The subexpressions

$$\psi^\dagger_{N_t}\hat{M}\frac{\partial\psi_{N_t}}{\partial a_p}, \quad \psi^\dagger_{N_t}\hat{M}\frac{\partial\psi_{N_t}}{\partial b_p} \tag{C7}$$

are of the same form as Eq. (C2), and hence can be calculated in the similar way. Setting $\hat{L}_{1,n} = -i\hat{H}(t_n)\Delta t/\hbar$, $\hat{L}_{2,n} = -i\hat{H}(t_n + (\Delta t)/2)\Delta t/\hbar$, $\hat{L}_{3,n} = -iH(t_{n+1})\Delta t/\hbar$,

$$T_{\rm Re} = -\frac{i}{\hbar}(\Delta t)\tilde{H}_{\rm d,Re}, \tag{C8a}$$

$$T_{\rm Im} = -\frac{i}{\hbar}(\Delta t)\tilde{H}_{\rm d,Im} \tag{C8b}$$

makes is possible to reuse the derivations of Ref. [47] to evaluate Eq. (C7). Similar to the master equation, $\frac{\partial P}{\partial\Delta_{\rm avg}}$ can be calculated by replacing $T_{\rm Re}$ or $T_{\rm Im}$ with

$$T_{\Delta_{\rm avg}} = -\frac{i}{\hbar}(\Delta t)\tilde{H}_{\Delta_{\rm avg}}. \tag{C9}$$

APPENDIX D: CONTINUOUS-WAVE DRIVE SPIN AMPLIFICATION IN REALISTIC SYSTEMS

In this Appendix, we show that the imperfections commonly found in realistic spin ensembles make the weak continuous-wave pulses used in Refs. [17–19] perform suboptimally. At the end of this Appendix, we also consider the frequency-ramp pulse that is known to perform well for the adiabatic state preparation [39], but applied to the spin amplification, we found it to only work well for the amplification times that are much longer than the coherence times in the realistic spins.

To show the effect of each imperfection separately, the detailed models for the realistic spins are not used in this Appendix. The ensemble is chosen to be a 1D array of 16 spins. For the idealized nearest-neighbor transverse-field Ising model, we use the Hamiltonian (2) with $J_{\pm,jk} = 0$, $J_{z,jk} = J_z$, $J_z > 0$ when j and k are nearest neighbors, $J_{z,jk} = 0$ otherwise. The drive has a constant Rabi frequency $\Omega/J_z = 0.1$ with $f_j = 1$ and detunings $\Delta_j = 0$, where all spins have the same transition frequency. Unless noted otherwise, the localized initial state $|\psi_1\rangle = \hat{\sigma}_{+,j=1}|\psi_0\rangle$ will be used in this Appendix, with $j = 1$ being the end spin in 1D [17] and corner spin in 2D [19].

In 1D, the simple explanation of the spin amplification is as follows [17–19]. The interaction term $J_z\hat{\sigma}_{z,j}\hat{\sigma}_{z,k}$ (for the nearest-neighbor j and k) in the Hamiltonian (2) causes effective detunings. When each spin is in the ground state $|0_j\rangle$, the drive is effectively off resonant with the detuning $8J_z$ in the bulk and with $4J_z$ for the end spins. Note that there are factors of 2 here compared to Ref. [19]. One factor of 2 is from the term $(\Delta_j/2)\sigma_{z,j}$, and another one is because the summation over $J_{z,jk}\hat{\sigma}_{z,j}\hat{\sigma}_{z,k}$ in the Hamiltonian (2) double counts the interaction terms with $j > k$ and $j < k$. As soon as one spin is excited to the state $|1_j\rangle$, the detuning on the neighboring spins due to the interaction term vanishes, and hence a resonant drive can create further excitations. The additional excitations are created due to a propagating domain wall around the initial one.

This is reflected in the numerical simulations. As shown by the solid red curve in Fig. 7(a), putting a single excitation in the end spin, the number of excited spins increases. The amplification is stopped and then reversed due the propagating domain wall being reflected at the other end of the ensemble. The dashed green curve in Fig. 7(a) shows the effect of added pure dephasing, i.e., with $\gamma_d/J_z = 0.265$ and $\gamma = 0$ in the master equation (B2) (evaluated using the quantum trajectory method [46]). The dotted blue curve in Fig. 7(a) uses $\gamma_d/J_z = 0.265$ and $\gamma/J_z = 0.004$, i.e., both pure dephasing and population decay. The decay rates are chosen to approximately match T_1 and T_ϕ used for the persistent-current artificial atoms in the main text. Assuming that $J_z = 2\pi \times 40$ MHz, $T_1 = 1$ μs, and $T_\phi = 15$ ns, we have $\gamma/J_z = 1/(T_1 J_z) \approx 0.004$ and $\gamma_d/J_z = 1/(2T_\phi J_z) \approx 0.265$.

For the initial zero-excitation state, using $\gamma_d = \gamma = 0$ results in off-resonant Rabi oscillations where all the spins precess close to the state $|0_j\rangle$. This is shown in Fig. 7(b), where the additional complexity in the dynamics stems from including the spin-spin interactions. Importantly, the total excitation number is bounded for a given constant Ω. When the dephasing is added, it can be viewed as a continuous measurement of the spin state by the environment, and therefore even a small amplitude of the state $|1_j\rangle$ can lead to a steady accumulation of the number of excited spins. This accumulation happens faster for stronger drives, as they make the spins acquire a larger amplitude of the state $|1_j\rangle$. This is shown in Fig. 7(c) that was obtained using $\gamma_d/J_z = 0.265$ and $\gamma/J_z = 0.004$. In the contrast to the $\gamma_d = \gamma = 0$ case, the populations are increasing over time. Despite this, a larger Ω can improve $P_1 - P_0$. Doing the sweep over $\Omega \in [0.2, 2.4] \times J_z$ and $\Delta_{avg} \in [-5, 5] \times J_z$, we find maximum $P_1 - P_0 = 2.49$ for $\Omega/J_z = 0.4$ and $\Delta_{avg} = 0$. This is slightly better than $P_1 - P_0 = 1.69$ for $\Omega/J_z = 0.1$ [maximum of the dotted blue curve in Fig. 7(a)].

Even without decay and decoherence, deviations of the Hamiltonian (2) from the nearest-neighbor Ising model also reduce the quality of the spin amplification. This is illustrated in Fig. 7(d). The long-range interaction can be detrimental if the next-nearest-neighbor shift is larger than Ω. This puts a limitation on how weak Ω can be in practice. Assuming that $J_{z,jk} = J_z r_{jk}^{-6}$, the next-nearest-neighbor shift in 1D is $4|J_{z,jk}|/J_z = 1/16$ (with $r_{jk} = |j - k|$), and it is smaller than the chosen $\Omega/J_z = 0.1$, so that spin amplification still works, as shown by the dashed green curve in Fig. 7(d). However, for $J_{z,jk} = J_z r_{jk}^{-3}$, the next-nearest-neighbor shift is $4|J_{z,jk}|/J_z = 1/2$, which is larger than $\Omega/J_z = 0.1$, and this completely shuts down spin amplification. We do not show the latter case in Fig. 7(d), but it looks very similar to the dashed green curve in Fig. 8(d) that shows $J_{z,jk} = J_z r_{jk}^{-6}$ in 2D and will be discussed below.

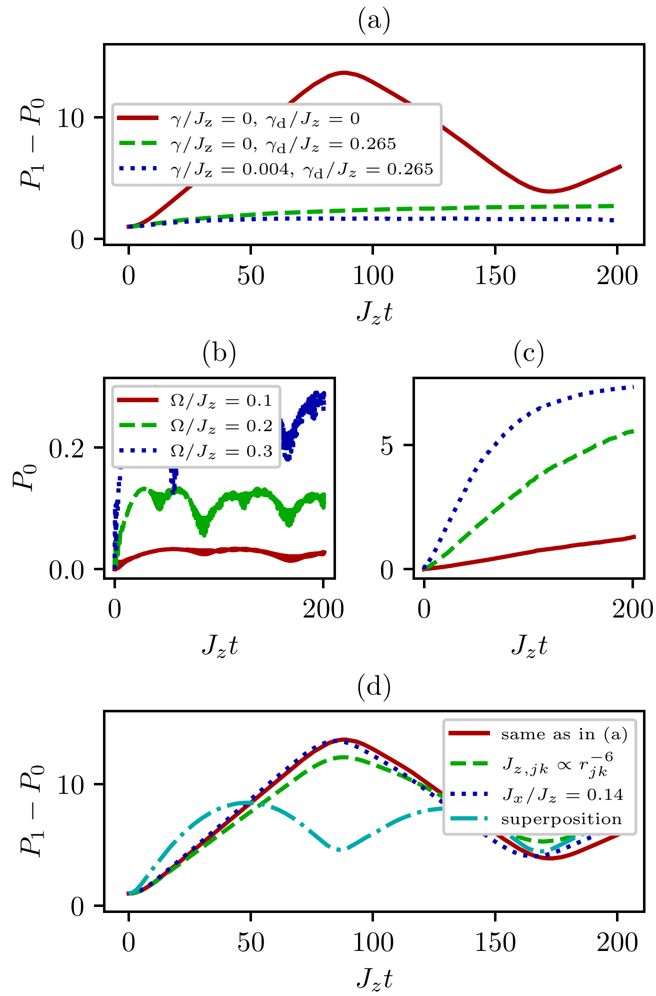

FIG. 7. (a) The differences of the excited spin populations P_1 and P_0 as functions of time. The 1D ensemble of 16 spins is described by the Hamiltonian (2) with $J_{\pm,jk} = 0$, nearest neighbor $J_{z,jk} = J_z$, $J_z > 0$, $\Omega/J_z = 0.1$ with $f_j = 1$, and $\Delta_j = 0$. For P_1, the initial state is with a single excitation in the end spin. (b), (c) Populations P_0 with the initial zero-excitation state as functions of time. The parameters are the same as in panel (a), except for Ω. (b) Using $\gamma_d = \gamma = 0$. Rapid oscillations make the curves appear to change thickness. (c) Using $\gamma_d/J_z = 0.265$ and $\gamma/J_z = 0.004$. The curves with the nonzero γ_d or γ have discontinuities due to using the quantum trajectory method with 500 trajectories instead of the master equation for the numerical calculations. (d) Using $\gamma_d = \gamma = 0$, but where the Hamiltonian is modified to either have a long-range $J_{z,jk} = J_z r_{jk}^{-6}$ with $r_{jk} = |j - k|$ (dashed green) or $J_x/J_z = 0.14$ (dotted blue). The dash-dotted cyan curve shows the effect of using the equal superposition state (4) as the initial one for P_1.

The long-range coupling $J_{z,jk} = J_z r_{jk}^{-3}$ is the asymptotic form of the dipole-dipole interaction of the persistent-current artificial atoms, but it has significant corrections when they are close to each other. It can be analytically evaluated using the Neumann formula for the mutual inductance. For the Rydberg atoms, the coupling $J_{z,jk} = J_z r_{jk}^{-6}$ is more natural. Regardless

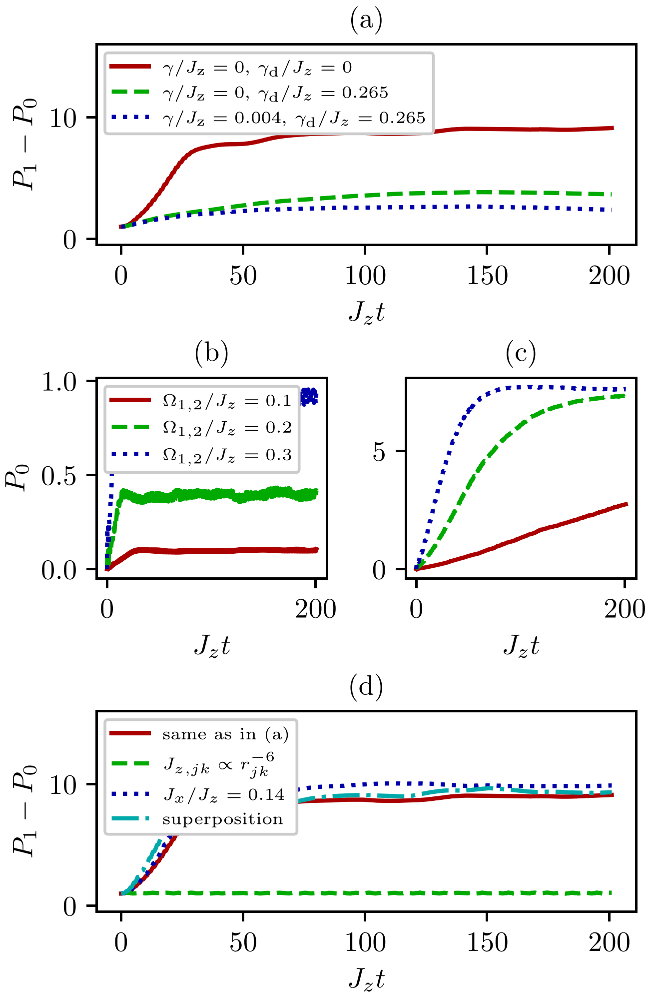

FIG. 8. This is the equivalent of Fig. 7, but where the 16 spins are arranged in a 2D square lattice instead of a 1D chain. (a), (d) The differences of the excited spin populations P_1 and P_0 as functions of time. (b), (c) Populations P_0 with the initial zero-excitation state. A two-frequency drive is used with the parametrization (9). The parameters are $\Omega_1/J_z = \Omega_2/J_z = 0.1$ [for panels (a) and (d)], $\Delta_{\mathrm{avg},1} = 0$, and $\Delta_{\mathrm{avg},2}/J_z = -4$.

of the power in the long-range interaction, it is possible to achieve some spin amplification by choosing a larger Ω [18] to compensate for the next-nearest-neighbor shifts and beyond. As discussed above, this will need to be balanced with the other imperfections that become more significant for larger Ω.

Another imperfection of the Hamiltonian shown in Fig. 7(d) is the nonzero $J_x/J_z = 0.14$ (dotted blue), which is approximately equal to the ratio calculated from the full model of the persistent-current artificial atoms for the chosen parameters. This also leads to a minor decrease in spin amplification. Finally, even if the Hamiltonian is the ideal nearest-neighbor Ising model, but the initial single-excitation state is a superposition of all the possible positions in the ensemble instead of being localized in the end spin, the continuous-wave drive spin amplification has a significantly lower maximum $P_1 - P_0$ (dash-dotted cyan).

The 2D version of the continuous-wave spin amplification is illustrated in Fig. 8. The intuitive explanation [19] builds

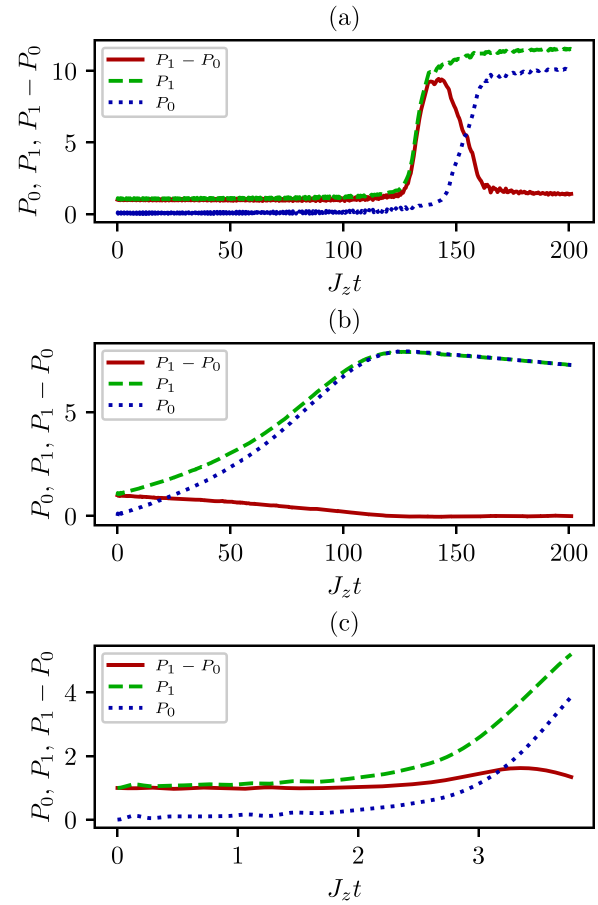

FIG. 9. Frequency-ramp protocol where Δ is changed linearly from $\Delta/J_z = 10$ to $\Delta/J_z = -10$ in the shown time interval. In all subplots, 16 spins are arranged in a 2D square lattice with $J_{z,jk} = J_z r_{jk}^{-6}$, $\Omega/J_z = 1$. (a) $\gamma/J_z = 0$, $\gamma_d/J_z = 0$ and (b) $\gamma/J_z = 0.004$, $\gamma_d/J_z = 0.265$. (c) Short amplification time with $\gamma/J_z = 0.004$ and $\gamma_d/J_z = 0.265$.

upon the one from the 1D case (described in the beginning of this Appendix). Again, accounting for factors of 2 resulting from the different scaling of the Δ_j terms and double counting of the $J_{z,jk}$ terms compared to Ref. [19], the argument is that in 2D, when all spins are in the ground state, the corner spins are effectively detuned by $8J_z$, the edge spins by $12J_z$, and the bulk spins by $16J_z$. This is due to the different number of the nearest neighbors that the spins in the different locations have. Setting the corner spin to the excited state makes the neighboring edge spins be detuned by only $4J_z$. Thus, introducing another drive with $\Delta_{\mathrm{avg},2} = -4J_z$ makes the edge spins become excited. Once they are, the neighboring bulk spins see their detuning effectively vanish, and hence the same resonant drive as for the 1D case can excite them. Thus, a two-frequency continuous-wave drive is sufficient to perform spin amplification in an idealized 2D ensemble.

There are some qualitative differences compared to the analysis of Ref. [19]. This is due to the fact that we simulate the full nearest-neighbor transverse-field Ising model with the exponential basis size of the Hilbert space instead of approximating it by an effective tunneling model with a reduced basis [19]. Because the ensemble has finite size, boundary effects make the amplification stop at around half of the maximal value $P_1 - P_0 = 16$. The achieved amplification stays at the same level in contrast with the 1D case where the total population starts decreasing again after the domain wall interacts with the boundary [cf. Fig. 7(a)]. There is also a more subtle difference in that the population of the initial corner spin decreases to around the same level as the steady state of the other spins in the ensemble. This is because we do not assume it to be of a different species with a different transition frequency like in Ref. [19]. The second drive frequency appears to be responsible for this population decrease, because it does not happen in 1D with a single-frequency drive.

The coherent deviations from the idealized model also have different behavior than in 1D [Fig. 8(d) compared to Fig. 7(d)]. Using the superposition state with the nearest-neighbor Hamiltonian has less difference in 2D (dash-dotted cyan curves). The 2D setup is more sensitive to the long-range interactions, however. This is because the next-nearest neighbors are closer in 2D than in 1D (across the diagonal instead of twice the distance in the same direction). Hence, even with $J_{z,jk} = J_z r_{jk}^{-6}$, the next-nearest-neighbor shift is $4|J_{z,jk}|/J_z = 1/2$, which is exactly the same as the next-nearest-neighbor shift for 1D with $J_{z,jk} = J_z r_{jk}^{-3}$. This shift is larger than $\Omega/J_z = 0.1$, and this prevents spin amplification from working.

A different pulse type, which was used for the adiabatic state preparation in Ref. [39], could also be applied here. In Fig. 9, Δ is changed linearly from $\Delta/J_z = 10$ to $\Delta/J_z = -10$ over the shown time interval. The 2D ensemble with $J_{z,jk} = J_z r_{jk}^{-6}$ is used to illustrate that this pulse type can handle the long-range interactions. The case with $\gamma_d = \gamma = 0$ is shown in Fig. 9(a) and results in maximal $P_1 - P_0 = 9.4$. However, once finite coherence time is added with $\gamma/J_z = 0.004$ and $\gamma_d/J_z = 0.265$, the difference $P_1 - P_0$ does not rise above the initial value of unity, as shown in Fig. 9(b). This is because the Δ-ramp time here is much larger than $1/\gamma_d = 3.77/J_z$. Changing Δ over this shorter time does not recover any meaningful $P_1 - P_0$, as shown in Fig. 9(c).

The failure of the Δ-ramp pulse can be understood from the fact that spin amplification is not a single-state transfer protocol. State transfer of any of the two initial states $|\psi_0\rangle$ and $|\psi_1\rangle$ [Eqs. (3) and (4)] is guaranteed by the adiabatic theorem and is robust to model imperfections, but spin amplification appears as a nonadiabatic effect where the Δ ramp needs to be stopped precisely when $|\psi_1\rangle$ is transferred to a highly excited state, but $|\psi_0\rangle$ is not, as Fig. 9(a) shows. For the realistic spins discussed in the main text, such a window of Δ values is narrow for the Rydberg atoms and does not exist at all for the persistent-current artificial atoms due to the strong dephasing and large inhomogeneity. The latter is illustrated by Figs. 9(b) and 9(c), albeit with a more idealized model than used in the main text for the persistent-current artificial atoms.

[1] F. Arute *et al.*, Hartree-Fock on a superconducting qubit quantum computer, Science **369**, 1084 (2020).

[2] S. Ebadi, T. T. Wang, H. Levine, A. Keesling, G. Semeghini, A. Omran, D. Bluvstein, R. Samajdar, H. Pichler, W. W. Ho, S. Choi, S. Sachdev, M. Greiner, V. Vuletić, and M. D. Lukin, Quantum phases of matter on a 256-atom programmable quantum simulator, Nature (London) **595**, 227 (2021).

[3] P. Scholl, M. Schuler, H. J. Williams, A. A. Eberharter, D. Barredo, K.-N. Schymik, V. Lienhard, L.-P. Henry, T. C. Lang, T. Lahaye, A. M. Läuchli, and A. Browaeys, Quantum simulation of 2D antiferromagnets with hundreds of Rydberg atoms, Nature (London) **595**, 233 (2021).

[4] Y. Kim, A. Eddins, S. Anand, K. X. Wei, E. van den Berg, S. Rosenblatt, H. Nayfeh, Y. Wu, M. Zaletel, K. Temme, and A. Kandala, Evidence for the utility of quantum computing before fault tolerance, Nature (London) **618**, 500 (2023).

[5] G. Bornet, G. Emperauger, C. Chen, B. Ye, M. Block, M. Bintz, J. A. Boyd, D. Barredo, T. Comparin, F. Mezzacapo, T. Roscilde, T. Lahaye, N. Y. Yao, and A. Browaeys, Scalable spin squeezing in a dipolar Rydberg atom array, Nature (London) **621**, 728 (2023).

[6] W. J. Eckner, N. Darkwah Oppong, A. Cao, A. W. Young, W. R. Milner, J. M. Robinson, J. Ye, and A. M. Kaufman, Realizing spin squeezing with Rydberg interactions in an optical clock, Nature (London) **621**, 734 (2023).

[7] J. Franke, S. R. Muleady, R. Kaubruegger, F. Kranzl, R. Blatt, A. M. Rey, M. K. Joshi, and C. F. Roos, Quantum-enhanced sensing on optical transitions through finite-range interactions, Nature (London) **621**, 740 (2023).

[8] J. A. Hines, S. V. Rajagopal, G. L. Moreau, M. D. Wahrman, N. A. Lewis, O. Marković, and M. Schleier-Smith, Spin squeezing by Rydberg dressing in an array of atomic ensembles, Phys. Rev. Lett. **131**, 063401 (2023).

[9] E. H. Chen, T. J. Yoder, Y. Kim, N. Sundaresan, S. Srinivasan, M. Li, A. D. Córcoles, A. W. Cross, and M. Takita, Calibrated decoders for experimental quantum error correction, Phys. Rev. Lett. **128**, 110504 (2022).

[10] Y. Zhao *et al.*, Realization of an error-correcting surface code with superconducting qubits, Phys. Rev. Lett. **129**, 030501 (2022).

[11] R. Acharya *et al.*, Suppressing quantum errors by scaling a surface code logical qubit, Nature (London) **614**, 676 (2023).

[12] W. Dreves, H. Jänsch, E. Koch, and D. Fick, Production of atomic alkali-metal beams in single hyperfine sublevels, Phys. Rev. Lett. **50**, 1759 (1983).

[13] S. C. Benjamin, Schemes for parallel quantum computation without local control of qubits, Phys. Rev. A **61**, 020301(R) (2000).

[14] S. C. Benjamin, Quantum computing without local control of qubit-qubit interactions, Phys. Rev. Lett. **88**, 017904 (2001).

[15] F. Mintert and C. Wunderlich, Ion-trap quantum logic using long-wavelength radiation, Phys. Rev. Lett. **87**, 257904 (2001).

[16] J. Fitzsimons and J. Twamley, Globally controlled quantum wires for perfect qubit transport, mirroring, and computing, Phys. Rev. Lett. **97**, 090502 (2006).

[17] J.-S. Lee and A. K. Khitrin, Stimulated wave of polarization in a one-dimensional Ising chain, Phys. Rev. A **71**, 062338 (2005).

[18] G. B. Furman, S. D. Goren, J.-S. Lee, A. K. Khitrin, V. M. Meerovich, and V. L. Sokolovsky, Stimulated wave of polarization in spin chains, Phys. Rev. B **74**, 054404 (2006).

[19] T. Close, F. Fadugba, S. C. Benjamin, J. Fitzsimons, and B. W. Lovett, Rapid and robust spin state amplification, Phys. Rev. Lett. **106**, 167204 (2011).

[20] A. W. Glaetzle, K. Ender, D. S. Wild, S. Choi, H. Pichler, M. D. Lukin, and P. Zoller, Quantum spin lenses in atomic arrays, Phys. Rev. X **7**, 031049 (2017).

[21] F. Cesa and H. Pichler, Universal quantum computation in globally driven Rydberg atom arrays, Phys. Rev. Lett. **131**, 170601 (2023).

[22] S. M. Patomäki, M. F. Gonzalez-Zalba, M. A. Fogarty, Z. Cai, S. C. Benjamin, and J. J. L. Morton, Pipeline quantum processor architecture for silicon spin qubits, npj Quantum Inf. **10**, 31 (2024).

[23] C. Nill, A. Cabot, A. Trautmann, C. Groß, and I. Lesanovsky, Avalanche terahertz photon detection in a Rydberg tweezer array, Phys. Rev. Lett. **133**, 073603 (2024).

[24] P. Cappellaro, J. Emerson, N. Boulant, C. Ramanathan, S. Lloyd, and D. G. Cory, Spin amplifier for single spin measurement, in *Quantum Computing in Solid State Systems*, edited by B. Ruggiero, P. Delsing, C. Granata, Y. Pashkin, and P. Silvestrini (Springer, New York, NY, 2006), pp. 306–312.

[25] A. Yoshinaga, M. Tatsuta, and Y. Matsuzaki, Entanglement-enhanced sensing using a chain of qubits with always-on nearest-neighbor interactions, Phys. Rev. A **103**, 062602 (2021).

[26] R. Coldea, D. A. Tennant, E. M. Wheeler, E. Wawrzynska, D. Prabhakaran, M. Telling, K. Habicht, P. Smeibidl, and K. Kiefer, Quantum criticality in an Ising chain: Experimental evidence for emergent E_8 symmetry, Science **327**, 177 (2010).

[27] T. P. Orlando, J. E. Mooij, L. Tian, C. H. van der Wal, L. S. Levitov, S. Lloyd, and J. J. Mazo, Superconducting persistent-current qubit, Phys. Rev. B **60**, 15398 (1999).

[28] R. Harris, T. Lanting, A. J. Berkley, J. Johansson, M. W. Johnson, P. Bunyk, E. Ladizinsky, N. Ladizinsky, T. Oh, and S. Han, Compound Josephson-junction coupler for flux qubits with minimal crosstalk, Phys. Rev. B **80**, 052506 (2009).

[29] A. P. M. Place *et al.*, New material platform for superconducting transmon qubits with coherence times exceeding 0.3 milliseconds, Nat. Commun. **12**, 1779 (2021).

[30] C. Wang *et al.*, Towards practical quantum computers: Transmon qubit with a lifetime approaching 0.5 milliseconds, npj Quantum Inf. **8**, 3 (2022).

[31] A. Somoroff, Q. Ficheux, R. A. Mencia, H. Xiong, R. Kuzmin, and V. E. Manucharyan, Millisecond coherence in a superconducting qubit, Phys. Rev. Lett. **130**, 267001 (2023).

[32] M. Tuokkola, Y. Sunada, H. Kivijärvi, J. Albanese, L. Grönberg, J.-P. Kaikkonen, V. Vesterinen, J. Govenius, and M. Möttönen, Methods to achieve near-millisecond energy relaxation and dephasing times for a superconducting transmon qubit, Nat. Commun. **16**, 5421 (2025).

[33] K. Kakuyanagi, Y. Matsuzaki, C. Déprez, H. Toida, K. Semba, H. Yamaguchi, W. J. Munro, and S. Saito, Observation of collective coupling between an engineered ensemble of macroscopic artificial atoms and a superconducting resonator, Phys. Rev. Lett. **117**, 210503 (2016).

[34] X. Ma *et al.*, Native approach to controlled-*Z* gates in inductively coupled fluxonium qubits, Phys. Rev. Lett. **132**, 060602 (2024).

[35] T. Chang, I. Holzman, T. Cohen, B. C. Johnson, D. N. Jamieson, and M. Stern, Reproducibility and gap control of superconducting flux qubits, Phys. Rev. Appl. **18**, 064062 (2022).

[36] M. D. Lukin, *Colloquium:* Trapping and manipulating photon states in atomic ensembles, Rev. Mod. Phys. **75**, 457 (2003).

[37] K. Hammerer, A. S. Sørensen, and E. S. Polzik, Quantum interface between light and atomic ensembles, Rev. Mod. Phys. **82**, 1041 (2010).

[38] C. Brif, R. Chakrabarti, and H. Rabitz, Control of quantum phenomena: Past, present and future, New J. Phys. **12**, 075008 (2010).

[39] A. Omran, H. Levine, A. Keesling, G. Semeghini, T. T. Wang, S. Ebadi, H. Bernien, A. S. Zibrov, H. Pichler, S. Choi, J. Cui, M. Rossignolo, P. Rembold, S. Montangero, T. Calarco, M. Endres, M. Greiner, V. Vuletić, and M. D. Lukin, Generation and manipulation of Schrödinger cat states in Rydberg atom arrays, Science **365**, 570 (2019).

[40] N. Lambert, Y. Matsuzaki, K. Kakuyanagi, N. Ishida, S. Saito, and F. Nori, Superradiance with an ensemble of superconducting flux qubits, Phys. Rev. B **94**, 224510 (2016).

[41] F. Motzoi, J. M. Gambetta, S. T. Merkel, and F. K. Wilhelm, Optimal control methods for rapidly time-varying Hamiltonians, Phys. Rev. A **84**, 022307 (2011).

[42] R. W. Heeres, P. Reinhold, N. Ofek, L. Frunzio, L. Jiang, M. H. Devoret, and R. J. Schoelkopf, Implementing a universal gate set on a logical qubit encoded in an oscillator, Nat. Commun. **8**, 94 (2017).

[43] C. Ding, M. Di Federico, M. Hatridge, A. Houck, S. Leger, J. Martinez, C. Miao, D. Schuster I, L. Stefanazzi, C. Stoughton, S. Sussman, K. Treptow, S. Uemura, N. Wilcer, H. Zhang, C. Zhou, and G. Cancelo, Experimental advances with the QICK (quantum instrumentation control kit) for superconducting quantum hardware, Phys. Rev. Res. **6**, 013305 (2024).

[44] See the specifications of the acousto-optic modulators at, e.g., https://www.sintec.sg.

[45] P. Doria, T. Calarco, and S. Montangero, Optimal control technique for many-body quantum dynamics, Phys. Rev. Lett. **106**, 190501 (2011).

[46] A. J. Daley, Quantum trajectories and open many-body quantum systems, Adv. Phys. **63**, 77 (2014).

[47] I. Iakoupov and K. Koshino, Saturable Purcell filter for circuit quantum electrodynamics, Phys. Rev. Res. **5**, 013148 (2023).

[48] J. Nocedal, Updating quasi-Newton matrices with limited storage, Math. Comput. **35**, 773 (1980).

[49] N. Khaneja, T. Reiss, C. Kehlet, T. Schulte-Herbrüggen, and S. J. Glaser, Optimal control of coupled spin dynamics: Design of NMR pulse sequences by gradient ascent algorithms, J. Magn. Reson. **172**, 296 (2005).

[50] Z.-J. Chen, H. Huang, L. Sun, Q.-X. Jie, J. Zhou, Z. Hua, Y. Xu, W. Wang, G.-C. Guo, C.-L. Zou, L. Sun, and X.-B. Zou, Robust and optimal control of open quantum systems, Sci. Adv. **11**, eadr0875 (2025).

[51] S. Günther, N. A. Petersson, and J. L. DuBois, Quandary: An open-source C++ package for high-performance optimal control of open quantum systems, in *2021 IEEE/ACM Second International Workshop on Quantum Computing Software (QCS)* (IEEE, New York, 2021), pp. 88–98.

[52] J. Somlói, V. A. Kazakov, and D. J. Tannor, Controlled dissociation of I_2 via optical transitions between the X and B electronic states, Chem. Phys. **172**, 85 (1993).

[53] R. Eitan, M. Mundt, and D. J. Tannor, Optimal control with accelerated convergence: Combining the Krotov and quasi-Newton methods, Phys. Rev. A **83**, 053426 (2011).
[54] R. Kosloff, S. Rice, P. Gaspard, S. Tersigni, and D. Tannor, Wavepacket dancing: Achieving chemical selectivity by shaping light pulses, Chem. Phys. **139**, 201 (1989).
[55] D. R. Jones, C. D. Perttunen, and B. E. Stuckman, Lipschitzian optimization without the Lipschitz constant, J. Optim. Theory Appl. **79**, 157 (1993).
[56] S. G. Johnson, The NLopt nonlinear-optimization package 2020, https://github.com/stevengj/nlopt.
[57] M. Hatridge, R. Vijay, D. H. Slichter, J. Clarke, and I. Siddiqi, Dispersive magnetometry with a quantum limited SQUID parametric amplifier, Phys. Rev. B **83**, 134501 (2011).
[58] F. Ceccarelli, G. Acconcia, A. Gulinatti, M. Ghioni, I. Rech, and R. Osellame, Recent advances and future perspectives of single-photon avalanche diodes for quantum photonics applications, Adv. Quantum Technol. **4**, 2000102 (2021).
[59] S. R. Muleady, M. Yang, S. R. White, and A. M. Rey, Validating phase-space methods with tensor networks in two-dimensional spin models with power-law interactions, Phys. Rev. Lett. **131**, 150401 (2023).
[60] M. Werninghaus, D. J. Egger, F. Roy, S. Machnes, F. K. Wilhelm, and S. Filipp, Leakage reduction in fast superconducting qubit gates via optimal control, npj Quantum Inf. **7**, 14 (2021).
[61] I. Iakoupov, Code and data for the paper "Spin amplification in realistic systems", Zenodo, 2026, https://doi.org/10.5281/zenodo.21715595.
[62] A. Maassen van den Brink, Hamiltonian for coupled flux qubits, Phys. Rev. B **71**, 064503 (2005).
[63] T. L. Robertson, B. L. T. Plourde, P. A. Reichardt, T. Hime, C.-E. Wu, and J. Clarke, Quantum theory of three-junction flux qubit with non-negligible loop inductance: Towards scalability, Phys. Rev. B **73**, 174526 (2006).
[64] T. Yamamoto, K. Inomata, K. Koshino, P.-M. Billangeon, Y. Nakamura, and J. Tsai, Superconducting flux qubit capacitively coupled to an LC resonator, New J. Phys. **16**, 015017 (2014).
[65] F. Yan, S. Gustavsson, A. Kamal, J. Birenbaum, A. P. Sears, D. Hover, T. J. Gudmundsen, D. Rosenberg, G. Samach, S. Weber, J. L. Yoder, T. P. Orlando, J. Clarke, A. J. Kerman, and W. D. Oliver, The flux qubit revisited to enhance coherence and reproducibility, Nat. Commun. **7**, 12964 (2016).
[66] M. Kamon, M. Tsuk, and J. White, FASTHENRY: A multipole-accelerated 3-D inductance extraction program, IEEE Trans. Microwave Theory Tech. **42**, 1750 (1994).
[67] S. R. Whiteley, XicTools, 2020, https://github.com/wrcad/xictools.
[68] K. Steinberg, M. Scheffler, and M. Dressel, Quasiparticle response of superconducting aluminum to electromagnetic radiation, Phys. Rev. B **77**, 214517 (2008).
[69] H. Duan, V. R. Manfrinato, J. K. W. Yang, D. Winston, B. M. Cord, and K. K. Berggren, Metrology for electron-beam lithography and resist contrast at the sub-10 nm scale, J. Vac. Sci. Technol. B **28**, C6H11 (2010).
[70] M. H. Devoret, Quantum fluctuations in electrical circuits, in *Fluctuations Quantiques/Quantum Fluctuations*, edited by S. Reynaud, E. Giacobino, and J. Zinn-Justin (Elsevier, Amsterdam, 1997), p. 351.
[71] U. Vool and M. Devoret, Introduction to quantum electromagnetic circuits, Int. J. Circuit Theory Appl. **45**, 897 (2017).